Parametric sub-structuring models of large space truss structures for structure/control co-design

Antonio Finozzi, Francesco Sanfedino, Daniel Alazard

▶ To cite this version:

Antonio Finozzi, Francesco Sanfedino, Daniel Alazard. Parametric sub-structuring models of large space truss structures for structure/control co-design. Mechanical Systems and Signal Processing, 2022, 180, pp.109427. ⟨10.1016/j.ymssp.2022.109427⟩. ⟨hal-03889558⟩

HAL Id: hal-03889558

https://hal.science/hal-03889558v1

Submitted on 8 Dec 2022

Parametric sub-structuring models of large space truss structures for structure/control co-design

A. Finozzi[1], F. Sanfedino [*,1], D. Alazard [*,1]

10 Avenue Edouard Belin, BP-54032, 31055, Toulouse, Cedex 4, France

Multidisciplinary optimization
Robust control
Truss structures
Flexible structure
Micro-vibrations

ABSTRACT

Modern and future high precision pointing space missions face increasingly high challenges related to the widespread use of large flexible structures. The development of new modeling tools which are able to account for the multidisciplinary nature of this problem becomes extremely relevant in order to meet both structure and control performance criteria. This paper proposes a novel methodology to analytically model large truss structures in a sub-structuring framework. A three dimensional unit cube element has been designed and validated with a Finite Element commercial software. This model is composed by multiple two-dimensional sub-mechanisms assembled using block-diagram models. This constitutes the building block for constructing complex truss structures by repetitions of the element. The accurate vibration description of the system and its minimal representation, as well as the possibility of accounting for parametric uncertainties in its mechanical parameters, make it an appropriate tool to perform robust Structure/Control co-design. In order to demonstrate the strengths of the proposed approach, a structure/control co-design study case is proposed and solved using structured robust H_∞-synthesis. The objective is to optimize the pointing performances of an antenna, minimizing the perturbations coming from the Solar Array Driving Mechanisms (SADM) of two solar panels, performing active control by means of multiple Proof Mass Actuators (PMA), and simultaneously reduce the mass of the truss-structure which connects the antenna to the main spacecraft body.

1. Introduction

In order to systematically face the challenges associated with the next generation of satellites, the European Space Agency (ESA) and NASA have combined their past experiences to cope with the fine pointing requirements of high accuracy observation and Science missions [1]. This represent a domain which is extremely multi-disciplinary: structural, control and system engineering considerations must coalesce to limit the propagation and amplification of internally generated disturbances through the satellite's flexible structures. For these reasons, the development of rigorous methodologies and design tools that can handle all these domains is crucial at early stages of design. The works of Preda et al. [2] and Sanfedino et al. [3,4] are example or this approach.

In the past decades, structural and control co-design has attracted a lot of attention due to its ability of merging these multiple multidisciplinary requirements into a single design flow. Moreover, the increasing use of large structures and appendages for Space applications has rendered flexible modal analysis mandatory for the design of proper spacecraft control laws.

---

[*] Corresponding authors.
E-mail addresses: antonio.finozzi@student.isae-supaero.fr (A. Finozzi), francesco.sanfedino@isae.fr (F. Sanfedino), daniel.alazard@isae.fr (D. Alazard).

[1] Institut Supérieur de l'Aéronautique et de l'Espace (ISAE-SUPAERO), Université de Toulouse

https://doi.org/10.1016/j.ymssp.2022.109427

In order to tackle the non-trivial modeling and analysis of these large and complex space systems, a sub-structuring technique using a multi-body approach is often considered to conceptually simplify the model. Seeing the overall structure as an assembly of multiple simpler sub-systems with increasing complexity has also the advantages of handling different types of boundary conditions at block assemblage level and easing sub-system validation.

The wide use of this approach for space applications has raised a significant interest in the development of proper modeling techniques that can prove to be versatile enough to account for multiple multi-body configurations, ranging from open-loop chains to closed-loops mechanisms.

Many sub-structuring techniques can be found in literature. A common approach relies on approximations linked to the Finite Element Method (FEM) or the Assumed Modes Method (AMM) [5]. However, these methods are heavily influenced by the set of predetermined boundary conditions assigned to the model, which may be drastically variable, for example in mass time-varying systems. Nevertheless, the FEM is currently the most popular method in structural analysis and it has had a deep impact in almost all multi-body modeling methods, such as the transfer matrix (TM) method and the component modes synthesis (CMS).

The Transfer Matrix (TM) Method, introduced by Holzer [6] and later independently by Myklestad [7] creates a transfer matrix that links up the state vectors (generalized accelerations and forces) of the two extremities of the flexible body. These methods are particularly well suited for serially connected bodies and open-chain structures. Their major drawback is the inversion problems of the matrices composing the model [8], whose matrices may be non-square or non-invertible depending on the boundary conditions. Moreover, these approaches are not optimal for a multi-body tree-like structures, where multiple inputs and multiple outputs are required at each end of the model [9]. This drawback is particularly significant for space applications, where multiple bodies and flexible appendages, such as antennas and solar panels, are attached to a central spacecraft body.

Component mode synthesis (CMS) approaches has been quite popular in the modeling of multi-body systems [10–12] thanks to matrix condensation reduction, which render this method particularly suited for sub-structuring problems [13–15]. However, in this approach, the sub-component matrices overlap with each other to create a complex model, difficult to understand to extend to systems with varying sizing parameters.

Methods based on effective mass/inertia of the appendages [16] and effective impedance matrix [17] represent another viable option to represent multi-body systems and have had significant space applications in [18–20] for attitude control purposes. These methods, however, lose the complete vibration behavior description of the systems, as they aim at delivering only the dynamic relation of state variable at the appendage root point. The application of these methods to design chain-like mechanisms is therefore not possible.

The Two-Input-Two-Output Port (TITOP) Model, a direct dynamic approach initially proposed in [21], overcomes these issues. The structure is conceived as a minimal state–space transfer between the accelerations and wrenches at the extremity points of the appendage and embeds both the direct and inverse dynamics: the IN/OUT channels are easily numerically invertible to account for multiple boundary conditions. Moreover this approach in a block-diagram model permits the design of closed-chain multi-body systems for any boundary conditions by creating feedback loops and inverting IN/OUT channels. An analytical uniform beam model in the TITOP approach was proposed by Mural et al. [22], while Perez et al. [23,24] introduced model parametrization in the Linear Fractional Transformation (LFT) form for co-design and robust control applications. A complete formulation of the TITOP beam model was proposed by Chebbi et al. [25], who performed a rigorous comparison with the Euler–Bernoulli beam theory for all boundary conditions. This work provided the first application of the TITOP model with inverted channels, which was used to model the four-bar mechanism by assembling multiple TITOP blocks. Sanfedino et al. [26] validated the inversion operation not only for analytical TITOP models but also for numerical ones provided by FEM commercial software and then extended the TITOP formalism for N-Input-N-Output Port (NINOP) models.

All the models derived in TITOP approach have been implemented in the last release of the Satellite Dynamics Toolbox (SDT) [27,28], which allows the user to easily build models of multi-body systems, parametrized according to mechanical sizing parameters and uncertain parameters of each body or substructure, following and generalizing the first idea introduced in [29]. Such models are fully compliant with the MATLAB®routines of the Robust Control Toolbox [30] to perform parametric robust control design and analysis.

All previous work, however, dealt only with simple systems when considering closed-loop kinematic chains. The main contribution of this work is to present a novel methodology to analytically model complex truss structures in the TITOP sub-structuring approach. These 3D system models represent a new set of tools which can be used to perform Structure/Control co-design, as they accurately describe the vibration dynamics response of the flexible bodies and have a minimal representation, limiting the number of DOFs present in the model. In particular, following a procedure similar to the one found in [25], multiple TITOP elements are assembled to form complex mechanical systems that can later be re-assembled to form large scale structures: multiple two dimensional (2D) and three dimensional (3D) multi-body systems will be presented with the aim of assembling a cubic structural element. The latter represents the minimal model of a complex 3D structure which can be used as the building block for the construction of large space truss structures.

In order to showcase the strength of the proposed approach, this work proposes a case study to display the ability of these parametric models of performing robust Structure/Control co-design or integrated design as proposed in [31]. The dual optimization of the structural design and the control performance fits the framework of the Multidisciplinary Design Optimization (MDO), which originated from the work of Schmit and Haftka [32,33]. The multidisciplinary approach is used when conflicting optimizations objectives stem from different disciplines and when a classical sequential optimization may fail to find the global optima of the problem. This is the case for Structure/Control co-design problems, where usually structural optimization is performed before the control one, iterating the process multiple time. This can be a long process and convergence is not granted due to the concurrent nature of the two sub-problems: mass reduction can increase significantly the flexibility of the system, whose low frequency modes may interfere with the satellite's Attitude Control System (ACS), as seen in [34].

When an analytical model of the structure is available, the integration of the design variables as uncertain parameters opens the possibility of achieving control/structure co-design in a unique iteration, using the non-smooth techniques available in the robust structured H_∞ control framework [35], as shown in several aerospace applications [23,36,37]. A drawback of such a direct co-design is that it could provide a non-global optimal design, by risking to fall within one of the many local minima. On the other hand, this approach has the advantage to be very easy to implement and very efficient from the computational time point of view when the number of sizing parameters is not too high. This work uses this approach for the structure/control co-design problem presented in the case study.

The main contributions of this paper are:

- development of a sub-structured model fully parametrized by both mechanical sizing parameters and uncertain parameters, allowing the complex truss structure to be assembled by block-diagram interconnection,
- validation of a 3D-cube element by a detailed comparison with a NASTRAN model,
- co-design of a complex space truss structure holding an optical payload and of the LOS (Line Of Sight) stabilization controller using multiple PMAs.

This work must also be positioned in the field of the Control Structure Interactions (CSI) which motivates lots of contributions since the 90's with a particular emphasize on model uncertainties. In [38], G. Balas already addressed the control of an experimental flexible truss structure (named Caltech Flexible Structure) using PMAs with a deep insight on the quantization of the uncertainties between the mathematical (or knowledge-based) model and the physical model. Uncertainties is also largely addressed in [39] and discussed on the MACE (Middeck Active Control Experiment) considering the impact of the suspension system required under 1-g environment on the system dynamical behavior under 0-g environment. A first toolbox for Uncertainty Bound IDentification (UBID) was proposed in [40]. More generally, such uncertainty quantization was required to feed robust control and analysis methods. The robust control design methods available till 2010 addressed only the full order design (i.e. the optimal controller have the same order than the design model). Thus, one can also find many contributions on reduction and associated reduction error bounds to reduce the order of the design model (and therefore of the controller). Today, effective methods to design robust structured controllers [35] where the order and/or the structure of the controller can be fixed rekindle the debate. In the present work, the general guideline is to push the knowledge-based model as far as possible and to consider it as the design model even if this model is a high-order model with a complex dependence on uncertain (real) parameters. Such an approach can be justified in the context of control/structure co-design during early design phases [41] when ground-based experimental mock-ups are not available. In addition, in the field of space engineering, the experiments for controls/structure interactions are very sensitive to the 1 g environment or to the gravity compensation mechanisms.

After a brief introduction on the TITOP approach used to model a flexible appendage in Section 2, the modeling of all 2D mechanism is detailed in Section 2.1. The introduction and validation of the cubic structural element is performed in Section 2.2. The in-depth description of the co-design study case is performed in Section 3. Sections 3.1 to 3.3 presents the model of the whole system from the various sub-structures. Section 3.4 details the closed-loop control strategy. Sections 3.5 to 3.7 presents the control/structure co-design formulation, results and validation.

2. TITOP approach

Let us consider a flexible body $\mathcal{A}_i$ as seen in Fig. 1 (left) connected to a parent structure $\mathcal{A}_{i-1}$ at the point P and to a child structure $\mathcal{A}_{i+1}$ at the point C. The resulting TITOP model $\mathbf{D}_{PC}^{\mathcal{A}_i}(\mathrm{s})$, schematized in Fig. 1 (right), is a $\{12\times 12\}$ linear dynamic model whose inputs are:

- $\mathbf{W}_{\mathcal{A}_{i+1}/\mathcal{A}_i,C}$: the $\{6\times 1\}$ wrench (forces and torques) applied by the body $\mathcal{A}_{i+1}$ to $\mathcal{A}_i$ at point C;
- $\ddot{\mathbf{u}}_P$: the $\{6\times 1\}$ inertial acceleration (linear and angular) imposed by the parent body $\mathcal{A}_{i-1}$ at point P to $\mathcal{A}_i$;

and the *conjugated* outputs are:

- $\ddot{\mathbf{u}}_C$: the $\{6\times 1\}$ components of the inertial acceleration of point C;
- $\mathbf{W}_{\mathcal{A}_i/\mathcal{A}_{i-1},P}$: the $\{6\times 1\}$ wrench applied by $\mathcal{A}_i$ to the parent structure $\mathcal{A}_{i-1}$ at point P.

All these input/output variables are projected in the body frame. Thus, to lighten the notations, the projection frame is not mentioned in the various block-diagrams presented hereafter.

As described in [25], the state–space representation of $\mathbf{D}_{PC}^{\mathcal{A}_i}(\mathrm{s})$ can be directly built from the data (flexible mode frequencies, modal participation factors and modal shapes) of the *clamped at P - free at C* model of the body $\mathcal{A}_i$. Then channel inversion operations can be used to derive the model under different boundary conditions.

Let us denote $[\mathbf{M}(\mathrm{s})]^{-1_{\mathbf{I}}}$ the model $\mathbf{M}(\mathrm{s})$ where the channel numbered in the vector of indexes $\mathbf{I}$ are inverted following the procedure described in [25] (Appendix 1), then for instance:

- $[\mathbf{D}_{PC}^{\mathcal{A}_i}(\mathrm{s})]^{-1_{[\mathbf{1:6}]}}$ models the body $\mathcal{A}_i$ under the *clamped at P - clamped at C* boundary conditions,
- $[\mathbf{D}_{PC}^{\mathcal{A}_i}(\mathrm{s})]^{-1_{[1\,2\,3\,4\,6\,11]}}$ models the body $\mathcal{A}_i$ under the *pinned at P and C* boundary conditions. Both pinned axes are the **y**-axis of the body frame used to project the model (Fig. 1 (left)).

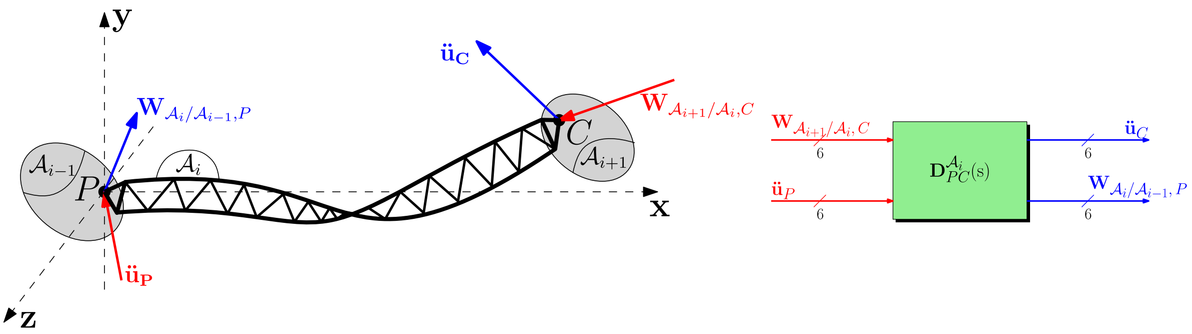

Fig. 1. TITOP scheme and nomenclature for a generic flexible appendage $\mathcal{A}_i$.

A multibody system composed of several flexible bodies and several revolute or clamped joints can then be built by the interconnection of the TITOP models of each body and the twice 6 × 6 DCM (Direction Cosine Matrix) between the various body frames. This approach was embedded in the Satellite Dynamics Toolbox (SDT) with various features:

- a NASTRAN/SDT interface to build the TITOP model directly from the output files (.f06 and .bdf) of the NASTRAN/PATRAN model,
- an analytical TITOP model of the EULER–BERNOULLI beam in the 6 d.o.fs (degree-of-freedom) case fully parametrized according to its length l (along the $\mathbf{x}$-axis of the beam reference frame), its section area S, its second moments of area I_z and I_y, its YOUNG modulus E and its mass density ρ. These parameters can be declared as varying parameters to obtain an LPV (Linear Parameter Varying) model fully compliant with the MATLAB®Robust Control Toolbox to perform robust design and performance analysis.

This beam model, fully detailed in [25], is used as the basic element for the truss structure models presented in the sequel. The reader is advised to read the SDTlib Users' Manual to have a deep insight in the SDT [28].

2.1. 2D mechanisms

In this section, a series of two-dimensional mechanisms is presented. The main goal of these kinematics is to act as intermediate step towards building complex three-dimensional structures. By exploiting the assembly of multiple elementary TITOP beam blocks, several multi-body mechanical systems have been implemented: the so called *L-Chain mechanism*, the *Triangle mechanism* and the *Square mechanism*. This section will detail the geometrical characteristics of these kinematics and their modeling using a block-diagram approach.

2.1.1. L-Chain mechanism

The L-Chain mechanism $\mathcal{L}$ is composed by two beams AB (body $\mathcal{A}_1$) and CB (body $\mathcal{A}_2$) connected at point B in a given angular configuration α, as seen in Fig. 2(a) (in the case $\alpha = \pi/2\,(rad)$). This mechanism is linked:

- to two parent bodies $\mathcal{B}_A$ and $\mathcal{B}_C$ at the point A and C, imposing accelerations $\ddot{\mathbf{u}}_A$ and $\ddot{\mathbf{u}}_C$,
- to a child body $\mathcal{B}_B$ at point B applying a wrench $\mathbf{W}_{\mathcal{B}_B/\mathcal{L},B}$.

The 3 input - 3 output ports model of the mechanism $\mathcal{L}$ is then described by the block-diagram depicted in Fig. 2(b). This model involves the *clamped at A - free at B* model $\mathbf{D}^{\mathcal{A}_1}_{A,B}(\mathrm{s})$ of the beam $\mathcal{A}_1$ and the *clamped at C - clamped at B* model $[\mathbf{D}^{\mathcal{A}_2}_{A,B}(\mathrm{s})]^{-1[1:6]}$ of the beam $\mathcal{A}_2$. The upper ports of these to sub-model are connected in a feedback loop to take into account:

- the loop closure constraint: the point B on the 2 bodies must have the same accelerations $\ddot{\mathbf{u}}_B$,
- the wrench balance at the point B of beam $\mathcal{A}_1$: $\mathbf{W}_{(\mathcal{A}_2+\mathcal{B}_B)/\mathcal{A}_1,B} = \mathbf{W}_{\mathcal{B}_B/\mathcal{L},B} - R_{2,1}\mathbf{W}_{\mathcal{A}_1/\mathcal{A}_2,B}$.

Note that in Fig. 2 the blocks $R_{i,j}$ correspond to the twice 6 × 6 DCM from the body frame of beam $\mathcal{A}_i$ to the body frame of beam $\mathcal{A}_j$.

This model is named *clamped–free–clamped (CFC) L-Chain* model and is denoted $\mathcal{L}^{CFC}(\mathrm{s})$. Indeed when the three inputs $\ddot{\mathbf{u}}_A$, $\mathbf{W}_{\mathcal{B}_B/\mathcal{T},B}$ and $\ddot{\mathbf{u}}_C$ (in this order) are null, the $\mathcal{L}$ mechanism is clamped at point A, free at point B and clamped at point C. This model described the dynamic behavior between three *conjugated* input–output pairs associated to the three ports (connection points) of the mechanism. Thus, using the channel inversion operation, one can also define:

$$\mathcal{L}^{CCC}(\mathrm{s}) = [\mathcal{L}^{CFC}(\mathrm{s})]^{-1[7:12]}, \quad \mathcal{L}^{FFC}(\mathrm{s}) = [\mathcal{L}^{CFC}(\mathrm{s})]^{-1[1:6]}, \ldots$$

All the inputs and outputs of the model $\mathcal{L}^{CFC}(\mathrm{s})$ are projected in the body frame $(\mathbf{x}_{\mathcal{L}},\ \mathbf{y}_{\mathcal{L}},\ \mathbf{z}_{\mathcal{L}})$ of the mechanism $\mathcal{L}$, chosen aligned with the frame of body $\mathcal{A}_1$ (see Fig. 2(a)).

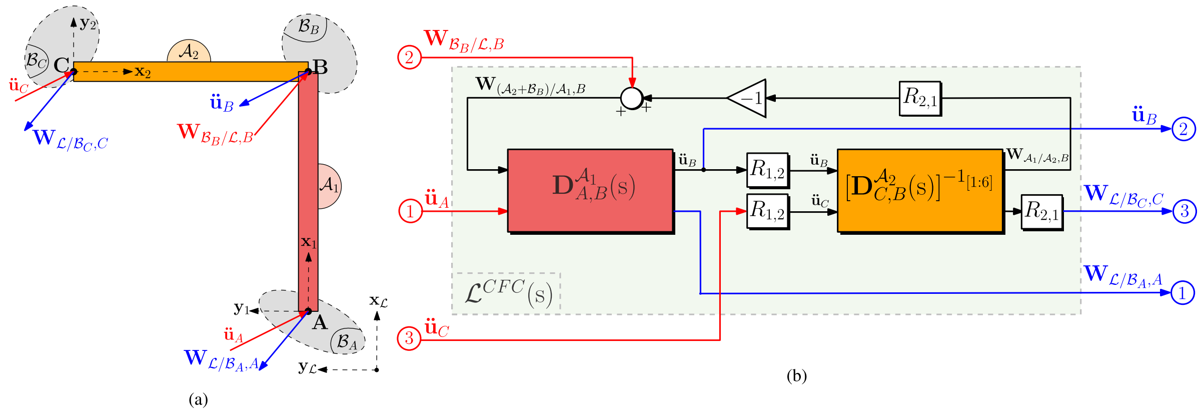

Fig. 2. Representation of the *Clamped–Free–Clamped* (CFC) L-Chain Mechanism $\mathcal{L}^{CFC}(s)$ (Fig. 3(a)) and its block-diagram model (Fig. 3(b)).

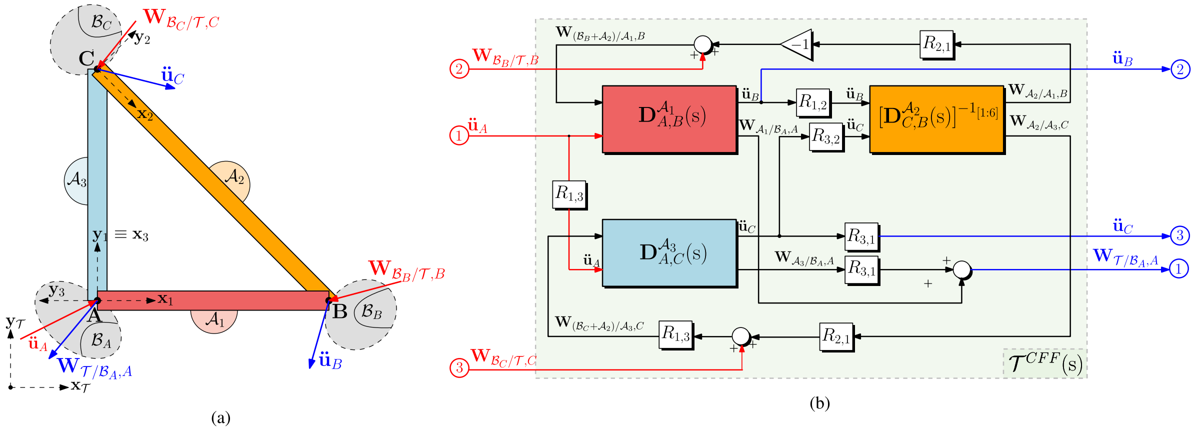

Fig. 3. Representation of the *Clamped–Free–Free* (CFF) Triangle Mechanism (Fig. 3(a)) and corresponding block-diagram model of the system (Fig. 3(b)).

2.1.2. Triangle mechanism

The modeling of a basic triangular closed-loop mechanism is hereby considered. This mechanism is first modeled in the *clamped at A, free at B, free at C* boundary conditions considering the acceleration $\ddot{\mathbf{u}}_A$, the wrenches $\mathbf{W}_{\mathcal{B}_B/\mathcal{T},B}$ and $\mathbf{W}_{\mathcal{B}_C/\mathcal{T},C}$ as inputs applied by the external bodies $\mathcal{B}_A$, $\mathcal{B}_B$ and $\mathcal{B}_C$ at points A, B and C, respectively (see Fig. 3(a)).

This model, denoted $\mathcal{T}^{CFF}(\mathrm{s})$ can then be represented by the block-diagram depicted in Fig. 3(b). Indeed, since the loop closure constraint at the point B is already taken into account in the model $\mathcal{L}^{CFC}(\mathrm{s})$ previously presented (considering now that $\alpha = \pi/4\,(rad)$), the model $\mathcal{T}^{CFF}(\mathrm{s})$ can be built by adding the model $\mathbf{D}^{\mathcal{A}_3}_{A,C}(\mathrm{s})$ of the third beam AC (body $\mathcal{A}_3$) connected to the model $\mathcal{L}^{CFC}(\mathrm{s})$ to satisfy the new constraints:

- the kinematic constraint: the point A on the 2 bodies $\mathcal{A}_1$ and $\mathcal{A}_3$ must have the same accelerations $\ddot{\mathbf{u}}_A$,
- the wrench balance at the point A: $\mathbf{W}_{\mathcal{T}/\mathcal{B}_A,A} = \mathbf{W}_{\mathcal{A}_1/\mathcal{B}_A,A} + R_{3,1}\mathbf{W}_{\mathcal{A}_3/\mathcal{B}_A,A}$,
- the wrench balance at the point C: $\mathbf{W}_{(\mathcal{B}_C+\mathcal{A}_2)/\mathcal{A}_3,C} = R_{1,3}\left(\mathbf{W}_{\mathcal{B}_C/\mathcal{T},C} + R_{2,1}\mathbf{W}_{\mathcal{A}_2/\mathcal{A}_3,C}\right)$.

All the inputs and outputs of this 3 input- 3 output port model $\mathcal{T}^{CFF}(\mathrm{s})$ are projected in the body frame ($\mathbf{x}_\mathcal{T}$, $\mathbf{y}_\mathcal{T}$, $\mathbf{z}_\mathcal{T}$) of the mechanism $\mathcal{T}$, chosen aligned with the frame of body $\mathcal{A}_1$ (see Fig. 3(a)).

2.1.3. Square mechanism

The square mechanism presented in Fig. 4 is composed of five beams: four of them form a polygonal perimeter and the last one is positioned diagonally to create two closed loop chains. This mechanism is modeled in the *clamped at A, free at B, free at C, free at C* boundary conditions considering the acceleration $\ddot{\mathbf{u}}_A$, the wrenches $\mathbf{W}_{\mathcal{B}_B/\mathcal{S},B}$, $\mathbf{W}_{\mathcal{B}_C/\mathcal{S},C}$ and $\mathbf{W}_{\mathcal{B}_D/\mathcal{S},D}$ as inputs applied by the external bodies $\mathcal{B}_A$, $\mathcal{B}_B$, $\mathcal{B}_C$ and $\mathcal{B}_D$ at points A, B, C and D, respectively (see Fig. 4(a)).

This model, denoted $\mathcal{S}^{CFFF}(\mathrm{s})$ can then be represented by the block-diagram depicted in Fig. 4(b). It involves directly the model $\mathcal{T}^{CFF}(\mathrm{s})$ of the triangular mechanism and the model $\mathcal{L}^{CFC}(\mathrm{s})$ of the L-chain mechanism with two feedback loops between their ports relative to the points B and C, allowing to take into kinematics constraints and wrench balances at these two connection points.

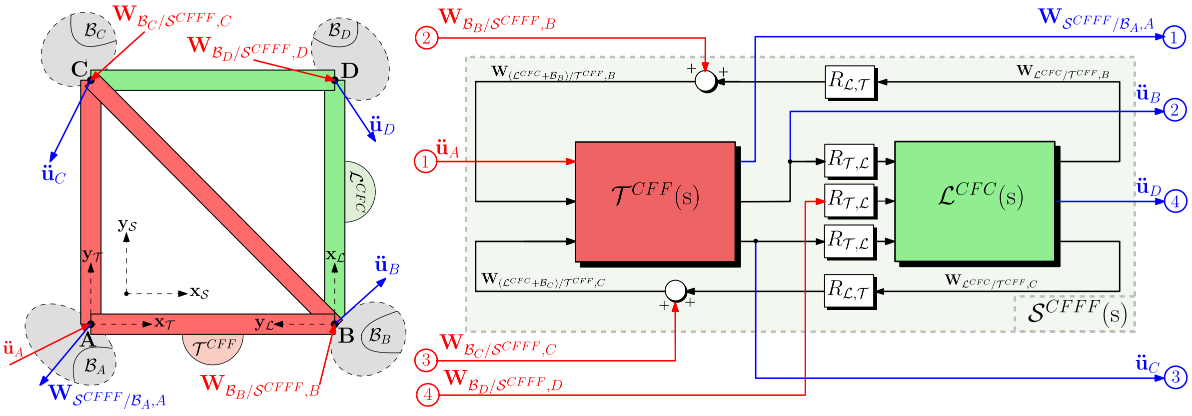

(a)

(b)

Fig. 4. Representation of the *Clamped–Free–Free–Free* (CFFF) Square Mechanism $\mathcal{S}^{CFFF}(\mathrm{s})$ (a) and corresponding block-diagram model of the system (b).

This allows for a drastic reduction in the assembly complexity: the model is composed only by two blocks while representing five flexible bodies in total. This showcases the power of this modular approach in structural design, whose advantages will be fully displayed in the three-dimensional approach introduced in Section 2.2.

All the inputs and outputs of this 4 input - 4 output port model $\mathcal{S}^{CFFF}(\mathrm{s})$ are projected in the body frame ($\mathbf{x}_\mathcal{S}$, $\mathbf{y}_\mathcal{S}$, $\mathbf{z}_\mathcal{S}$) of the mechanism $\mathcal{S}$, chosen aligned with the frame of the $\mathcal{T}$ mechanism (see Fig. 4(a)). Using the channel inversion operation, one can also defined:

$$\mathcal{S}^{CCCC}(\mathrm{s}) = [\mathcal{S}^{CFFF}(\mathrm{s})]^{-1_{[7:24]}} \ .$$

2.2. 3D Mechanisms

The two-dimensional elements introduced in Section 2.1 ans the channel inversion operation are powerful tools that can be used for the creation and assembly of complex three-dimensional structures. In the context of the multi-body approach followed in this paper, the mechanical conception focused on the definition of a unit-cube 3D module which could represent the basic building block for large space truss structures.

2.2.1. Cube mechanism

The Cube Mechanism $\mathcal{C}$ is a multi-body structure composed by 13 flexible appendages, assembled at 8 nodes to form a cubic outline with diagonal elements along the faces. A representation of its complex kinematics is given in Fig. 5(a). Each node i, $i = 1, \dots, 8$ of the cube is connected to an external body $\mathcal{B}_i$ imposing an acceleration $\ddot{\mathbf{u}}_{N_i}$ (case of a parent body) or applying a wrench $\mathbf{W}_{\mathcal{B}_i/\mathcal{C},N_i}$ (case of child body).

At a first glance, it can be noticed that no flexible appendix can be found to form the side of the bottom face of the Cube, along the (x, y) plane. This has been done to facilitate the construction of complex mechanical systems: this structure is conceived as a unit-cube-module which can be stacked on top of other elements, serially connecting them to create an elongated system. In the same fashion, multiple cubes can then be added on the sides as well. An example of this sub-structuring modeling technique will be outlined in the case study of Section 3.

In order to facilitate this serial connection of cubes along the z-axis, the design of this mechanical system has been carried out to present four lower nodes (from N_1 to N_4) with accelerations imposed on the structure by the external parent bodies $\mathcal{B}_i\,(i = 1, \dots, 4)$, while the upper nodes of the structure (from N_5 to N_8) are subjected to the wrenches transmitted by the external child bodies $\mathcal{B}_i\,(i = 5, \dots, 8)$. These excitation acting on the system, highlighted in red in Fig. 5(a), will represent the inputs of the 8 input - 8 output port model of the cube, denoted $\mathcal{C}^{CCCC-FFFF}(\mathrm{s})$. Following the general NINOP model formalism, the outputs are the *conjugate* of the inputs.

As it can be seen in Fig. 5(b), the model $\mathcal{C}^{CCCC-FFFF}(\mathrm{s})$ of this complex three-dimensional structure can be easily modeled by means of only two different 2D mechanisms: *Clamped–Free–Clamped (CFC)* L-Chains $\mathcal{L}_j^{CFC}(\mathrm{s})$, repeated four times, and one single *Clamped–Clamped–Clamped–Clamped (CCCC)* Square Mechanism $\mathcal{S}^{CCCC}(\mathrm{s})$. The imposed accelerations at nodes N_1 to N_4 have been inputted directly to the two *clamped* ends of the L-Chains, while their *free* vertex receives the combined effort of the external forces applied by $\mathcal{B}_i$ $(i = 5, \dots, 8)$, and $\mathcal{S}^{CCCC}(\mathrm{s})$. Exactly like in the previous cases, the feedback loops between the sub-blocks allows to satisfy the kinematics constraints and the wrench balances.

Finally, in Fig. 5(b) it can be noted that this model does not present DCM between the blocks. This is made possible by the fact that the changes of reference frames are handled internally within the elementary blocks, allowing the possibility to express all vectors in any generic common frame (for instance, the frame $(N_1, \mathbf{x}, \mathbf{y}, \mathbf{z})$ for the cube).

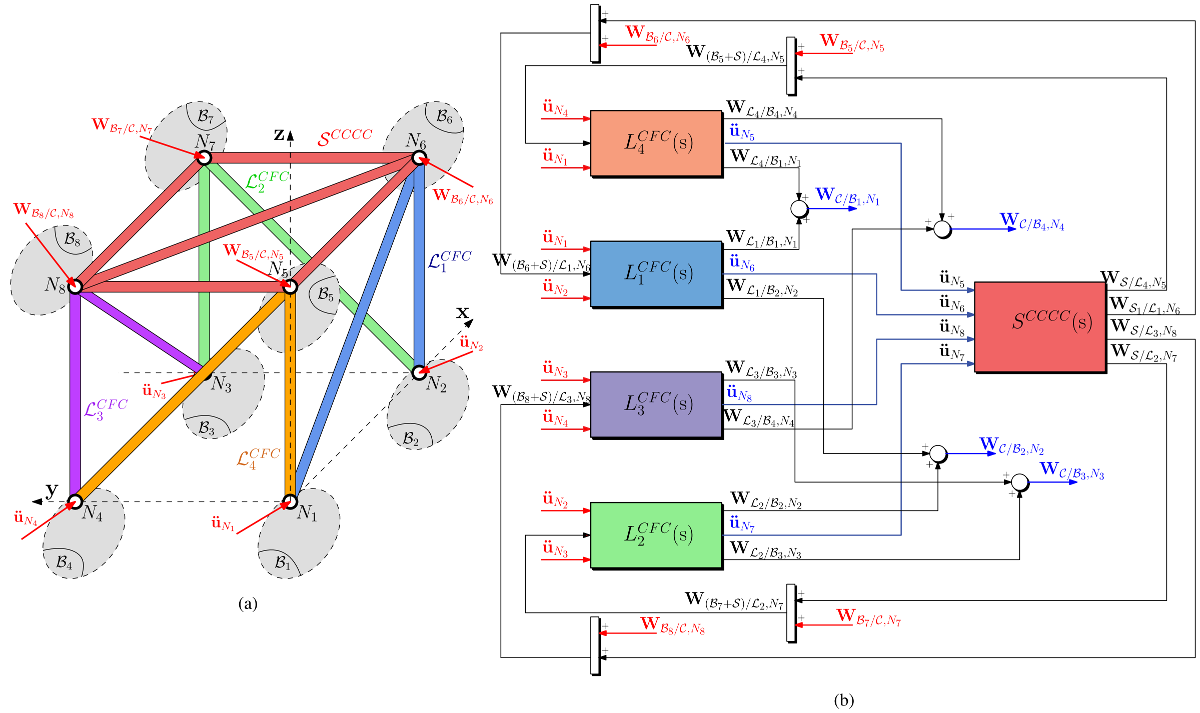

Fig. 5. Geometrical representation (a) and block diagram system (b) of the Cubic Element $\mathcal{C}$(s).

Table 1
Parameters of the cube sides and TITOP Beams used for the validation of Cube model.

l_x [m]	l_y [m]	l_z [m]	S [m^2]	ρ [kg/m^2]	E [GPa]	ν	I_y [m^{-4}]	I_z [m^{-4}]	ξ
1.0	1.0	1.0	9e–4	2700	70	0.35	6.75e–08	6.75e–08	0.001

2.2.2. System validation

The sub-structuring technique presented in the previous sections has been implemented in MATLAB®SIMULINK®in the form of N-Input-N-Output Port block models, which depict the dynamical behavior of each mechanism. These blocks integrate the analytical beam model of the SDT library [28].

These new models of elementary truss structures are now validated by comparison with the models obtained from a widespread finite-element-model commercial software: MSC Patran/Nastran. This validation is performed on the Cube structure. Since it embeds the three elementary (L-chain, Triangle and Square) sub-structures, the validation of the Cube model acts as a general validation of all its sub-structural components.

Geometry definition and Patran/Nastran modeling. A cube mechanism, as described in Section 2.2.1 is hereby considered for verification purposes. Its geometry is fixed by means of the length of its sides, l_x, l_y and l_z, along the axis of the (N_1, x, y, z) reference frame and by the mechanical characteristics of each appendage composing the kinematics. The same homogeneous beam has been repeated for each flexible body. The full mechanical characterization of the validation model is described by Table 1, where ν is the Poisson's coefficient and ξ is the damping factor.

For the comparison with the Nastran model, the cube is only clamped at node N_1 whose model (labeled *SDT*) is obtained using the channel inversion operation:

$$\mathcal{C}^{CFFF-FFFF}(\mathrm{s}) = [\mathcal{C}^{CCCC-FFFF}(\mathrm{s})]^{-1_{[7:24]}} .$$

That allows to compare not only the flexible mode frequencies but also their modal participation factors at this node.

The same mechanical system has been implemented in MSC/Patran, using the same mechanical characteristics of the *SDT* model and modeling each beam using the *CBEAM* element property, in order to take torsional behavior into account. The 3D model (labeled *Patran*) created in MSC/Patran is displayed in Fig. 6, where the 5 elements used for each beam can be distinguished. The structure can be seen clamped at the origin of the (x, y, z) axis, which corresponds to node N_1.

Table 2 describes the first ten modes of the two models (*SDT* and *Patran*) by means of their natural frequencies ω_k and their modal participation factors. The comparison shows a good match in both physical properties.

A more detailed validation is possible thanks to the interface between MSC/Nastran and SDT library which allows to import the MSC/Patran model directly in MATLAB®/SIMULINK®. From the Nastran `.f06` analysis file, this interface provides the 6 × 6

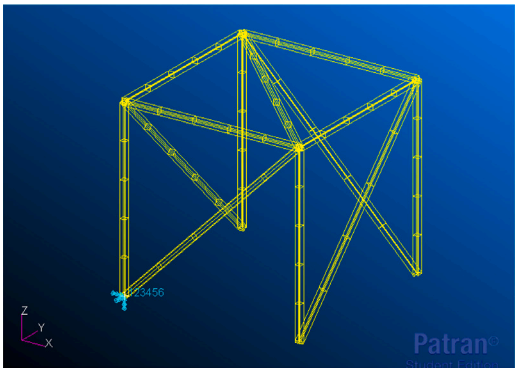

Fig. 6. Validation FEM model implemented in MSC/Patran.

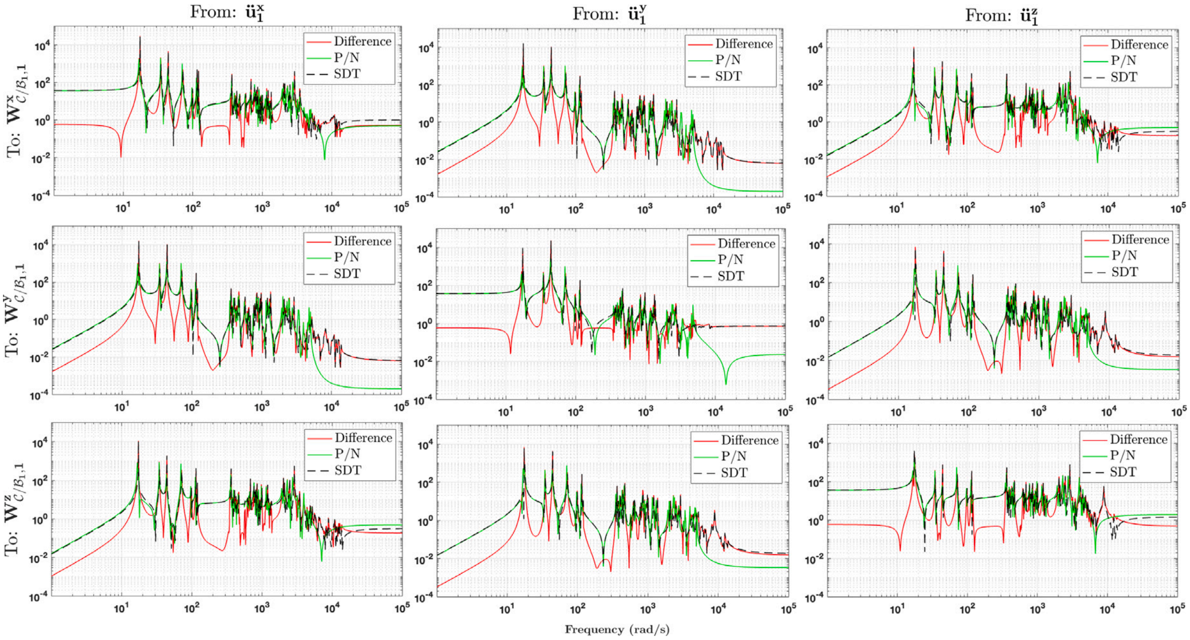

Fig. 7. Verification of the Cube element's frequency response (SDT) by comparison with the MSC Patran/Nastran model (P/N).

Table 2
Comparison between the Patran/Nastran model and the SDT cube: modal frequency ω_k and participation factors ($T_1, T_2, T_3, R_1, R_2, R_3$).

Mode	ω_k [rad/s]		*T1*		*T2*		*T3*		R1		R2		R3	
	Patran	*SDT*	*Patran*	*SDT*	*Patran*	*SDT*	*Patran*	*SDT*	*Patran*	*SDT*	*Patran*	*SDT*	*Patran*	*SDT*
1	16.77	17.43	−3.830	−3.912	2.040	2.207	1.714	1.474	0.113	−0.292	−3.746	−3.704	5.127	5.236
2	17.51	17.75	−0.716	−0.432	2.211	2.091	−3.890	−4.021	−5.495	−5.475	1.684	1.964	2.167	1.815
3	*34.37*	34.90	2.279	−2.271	1.111	−1.256	−0.993	0.921	0.069	−0.018	4.423	−4.315	*0.676*	−0.765
4	43.66	44.34	2.066	−2.004	4.546	−4.534	0.749	−0.824	−2.424	2.421	0.031	0.074	0.503	−0.439
5	70.36	72.18	1.711	−1.746	1.737	1.616	1.288	1.239	−0.897	−0.844	−0.677	−0.651	−0.128	−0.149
6	97.26	99.54	0.482	−0,428	0.402	−0.389	0.398	−0.392	−0.192	0.187	−0.079	0.086	0.007	−0.002
7	112.83	115.31	0.667	−0.656	0.401	−0.398	0.561	−0.567	−0.144	0.140	0.173	−0.168	0.129	−0.132
8	117.91	120.84	−0.554	−0.552	0.067	0.059	−0.074	−0.095	−0.026	−0.022	−0.005	−0.005	0.043	0.042
9	348.92	354.30	−0.184	−0.139	0.126	0.118	0.386	0.472	−0.034	−0.031	−0.071	−0.077	0.031	0.032
10	361.72	365.24	−0.727	−0.761	−0.108	−0.123	−1.101	−1.078	0.023	0.027	0.035	0.026	−0.042	−0.047

transfer from the acceleration $\ddot{\mathbf{u}}_{\mathbf{N_1}}$ at the node N_1 to the reaction wrench $\mathbf{W}_{\mathcal{C}/\mathcal{B}_1,\mathbf{N_1}}$ at this node. The frequency-domain response for the 3 translation degrees of freedom of this transfer is depicted in Fig. 7 (labeled *P/N*) and compared with the ones from the proposed model (labeled *SDT*). The analysis of these plots confirms a good match between the two models. In the $[0,\ \ 500]$ rad/s

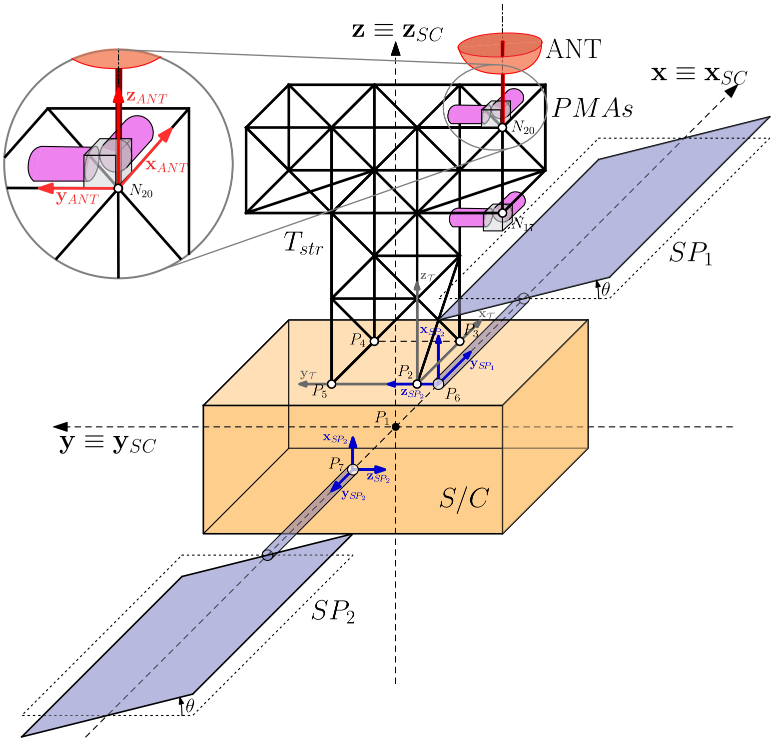

Fig. 8. Overall view of satellite's case study. The spacecraft composed by a main central spacecraft body (S/C), two Solar Panels (SP_1, SP_2) rotated around axis x of an angle θ. The HPP antenna (ANT) and the 4 PMAs are both placed on top of the truss structure T_{str}.

frequency range, the relative error on each transfer is below 5% except of course on the resonances which are not exactly at the same frequencies (see Table 2).

3. Application on space structural and control co-design study case

This section introduces a study case on a space application to demonstrate the power of the proposed multi-body sub-structuring approach for modeling and control of flexible structures. Let us consider a Telecom satellite having one High-Precision-Pointing (HPP) antenna connected to the main spacecraft (S/C) body by means of a large truss structure as in Fig. 8. Two Solar Panel Arrays are connected to the sides of the satellite and are able to rotate thanks to Solar Array Driving Mechanisms (SADM), which on the other hand introduce perturbations in the attitude of the spacecraft and in the pointing of the antenna.

In this context, the blocks introduced in Sections 2.1 and 2.2 have been used to construct the large T-Shaped truss structure T_{str}, which support the high-precision antenna. Given that the multi-body design is based on the TITOP beam model, this complex flexible system can be fully parametrized for any physical property characterizing the beams. A structural and robust control co-design has been implemented for the system, to showcase the strength of a parametric structural model by achieving the two following concurrent goals:

1. Reject the perturbations introduced by the SADMs acting on the Line-of-Sight (LOS) of the Antenna by performing an active control using 4 PMAs, distributed on the structure.
2. Minimize the mass of the T-Truss structure T_{str} by reducing the section of the beams composing the system, all while complying with the pointing and vibration rejection requirements.

The following sections will detail the design and assemblage of the T-Truss structure and the procedure chosen to implement the co-design.

3.1. Flexible T-Truss structure

The T-shaped Truss antenna support has been modeled by means of five Cube mechanism elements, connected to each other to form the structure seen in Fig. 9, where the diagonal beams on the faces have been hidden to facilitate reader's understanding of the

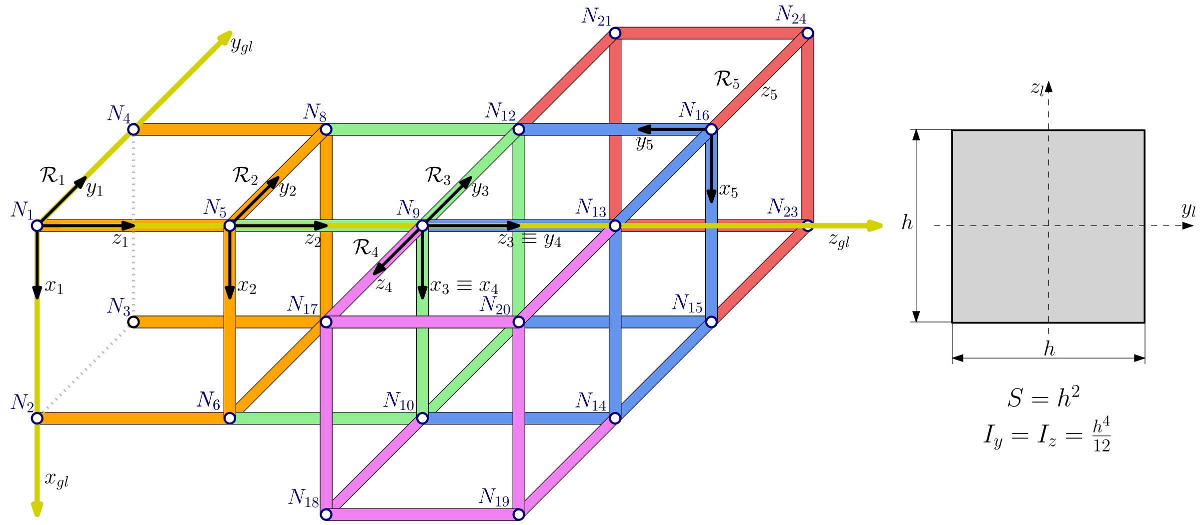

Fig. 9. Simplified representation of the T-Shaped Truss Structure, without any diagonal beam in the cubes' faces, and the beams square sections. For clarity sake, the Cube elements $\mathcal{C}_i$ are represented with their local reference frames $\mathcal{R}_i$ to indicate their orientation in the global reference frame $\mathcal{R}_{gl}(N_1,\ \mathbf{x}_{gl},\ \mathbf{y}_{gl},\ \mathbf{z}_{gl})$. The section area S and bending inertia I_y, I_z of each beam is expressed in the generic beam local reference of frame $\mathcal{R}_l(N_l,\ x_l,\ y_l,\ z_l)$ as function of the side parameter h.

Table 3
Parameters of TITOP Beams used for the T-Truss Structure.

$S\,[\text{m}^2]$	$\rho\,[\text{kg/m}^2]$	$E\,[\text{GPa}]$	ν	$I_y\,[\text{m}^{-4}]$	$I_z\,[\text{m}^{-4}]$	ξ
h^2	2700	70	0.35	$h^4/12$	$h^4/12$	0.001

architecture. Overall, this complex mechanical system is composed by 65 flexible beams. Among them, it is possible to identify a core assembly of three cubes ($\mathcal{C}_1$, $\mathcal{C}_2$ and $\mathcal{C}_3$) which are simply serially stacked on top of each other, along the $\mathbf{z}_{gl}$ axis on the global frame of reference (N_1, $\mathbf{x}_{gl}, \mathbf{y}_{gl}, \mathbf{z}_{gl}$). The remaining two cubes are then placed on the sides of the previous assembly, developing along the $\mathbf{y}_{gl}$ axis direction. This is achieved by the use of two direction cosine matrices, which perform a rotation of the cubes around the $\mathbf{x}_{gl}$ axis. This results in cube $\mathcal{C}_4$ facing towards the negative direction of $\mathbf{y}_{gl}$ while $\mathcal{C}_5$ towards the positive one.

The overall structure is composed by 24 nodes in total. Four of them – nodes from N_1 to N_4 – are connected to the S/C main body and therefore are designed to have an acceleration imposed onto them. The rest of the points on the other hand can receive an external input in the form of an external wrench.

This is the case for nodes N_{17} and N_{20}, where the PMAs and the antenna is connected, while no external forcing term are applied to other points of the structure. In terms of physical and geometrical characterization of the system, it has a total envelope of 1 m×3 m×3 m, with each single cube having a volume of 1 m×1 m×1 m. The same beam properties have been repeated for all the 65 beams composing the structure. Given an aluminum beam with a square section, a parametric model has been implemented by means of the section length h. This variable drives both the section area and the second moments of area of the beam, as displayed in Fig. 9. The parameter will then be at the center of the structural-control co-design of Section 3, as it is directly related to both mass and stiffness properties of the system. Finally, the mechanical characterization of all the beams is given in Table 3.

3.2. Proof Mass Actuators (PMAs) model

The PMA mechanical system has been modeled in Fig. 10 as the body $\mathcal{B}$, composed by a rigid casing and a one-dimensional spring–mass–damper system. Under these assumptions, the mechanical actuator is fully defined by the following set of parameters:

- $\mathcal{R}_a$: local reference frame attached to the PMA at the reference point O;
- $\mathbf{v}$: the unit vector along the PMA axis, expressed in $\mathcal{R}_a$;
- G and P: the center of mass of the PMA (at rest) and the connection point to the parent body, respectively;
- $M^{\mathcal{B}}$ and $\mathbf{I}_G^{\mathcal{B}}$: respectively, the mass and the inertia matrix at G of the PMA casing;
- m_p, k_p, d_p.: the mass, stiffness and damper of the spring–mass–damper system describing the dynamics of the PMA along the axis $\mathbf{v}$;
- u: control effort applied on the proof mass along the axis $\mathbf{v}$;
- δ_x. Relative displacement of the proof mass with respect to the casing;
- $\ddot{\mathbf{u}}_P$: $\{6 \times 1\}$ acceleration twist of the PMA at the connection point expressed in the $\mathcal{R}_a$ frame;

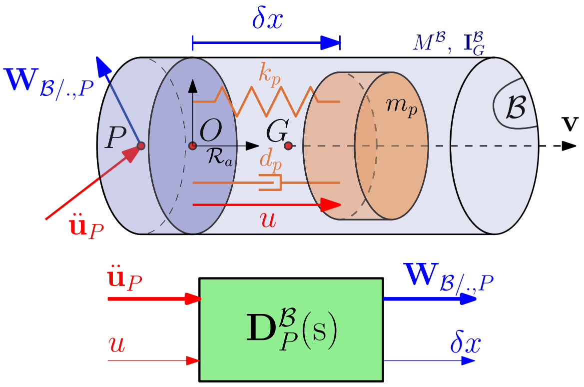

Fig. 10. PMA mechanical system and its associated block diagram system $\mathbf{D}_P^{\mathcal{B}}(\mathrm{s})$ in the TITOP approach.

- $\mathbf{W}_{\mathcal{B}/.,P}$: $\{6 \times 1\}$ wrench applied by the PMA at point P, expressed in the $\mathcal{R}_a$ frame;

The PMA mechanical system $\mathcal{B}$ has then been modeled as $\mathbf{D}_P^{\mathcal{B}}(\mathrm{s})$, a $\{7 \times 7\}$ linear dynamic model in the TITOP approach. The system is obtained by means of the governing equations of the mechanical dynamics, defined as follows:

$$m([\mathbf{v}^T \quad \mathbf{0}_{1\times3}]\ddot{\mathbf{u}}_G + \ddot{\delta}_x) = -k\delta_x - d\dot{\delta}_x + u \tag{1}$$

$$\ddot{\mathbf{u}}_G = \boldsymbol{\tau}_{\boldsymbol{GP}}\ddot{\mathbf{u}}_P \tag{2}$$

$$\mathbf{W}_{\mathcal{B}/.,P} = -\boldsymbol{\tau}_{\boldsymbol{GP}}^T \left(\begin{bmatrix} M\mathbf{I}_3 & \mathbf{0}_3 \\ \mathbf{0}_3 & \mathbf{I}_G^{\mathcal{B}} \end{bmatrix} \boldsymbol{\tau}_{\boldsymbol{GP}}\ddot{\mathbf{u}}_P + m \begin{bmatrix} \mathbf{v} \\ \mathbf{0} \end{bmatrix} \ddot{\delta}_x \right) \tag{3}$$

$$\boldsymbol{\tau}_{\boldsymbol{GP}} = \begin{bmatrix} \mathbf{I}_3 & [\mathbf{r}_{\mathbf{GP}}]_\times \\ \mathbf{0}_{3\times3} & \mathbf{I}_3 \end{bmatrix} \tag{4}$$

where $\boldsymbol{\tau}_{GP}$ is the *Kinematic Model* of the rigid link between point G and point P, defined thanks to the skew matrix $[\mathbf{r}_{GP}]_\times$ associated to the vector $\mathbf{r}_{GP}$ from node G to node P.

The PMA 7×7 block-diagram model $\mathbf{D}_P^{\mathcal{B}}(\mathrm{s})$ is showcased in Fig. 10. The first 6×6 port of the model defines the transfer between the acceleration $\ddot{\mathbf{u}}_P$ and the wrench $\mathbf{W}_{\mathcal{B}/.,P}$, while the last describes the one between the control effort u and the proof mass relative displacement δ_x. The mechanical parameters which describe the PMAs used in the current case study are given in appendix, Table 6.

3.3. System modelization

3.3.1. Full order Linear Parameter Varying (LPV) model

The complete system in Fig. 8 is modeled by means of a block-diagram approach using elements derived from the SDT library introduced in [28]. The block-diagram representation of the whole spacecraft is then depicted in Fig. 11 and is detailed by:

- *Central body (S/C).* This block is a static 42×42 multi-port rigid body model. It models the dynamics of a rigid body subjected to multiple wrenches applied at connection points P_1, the center of mass where is located the Attitude Control System (ACS), P_2, P_3, P_4, P_5 the 4 connection points with the T-truss structure, and P_6, P_7 the connection points with the 2 solar panels. The geometry of these points is detailed in Appendix, Table 7.
- *Solar Panels (SP_i, $i = 1, 2$).* These 2 blocks are 6-th order single port flexible body models. Each solar panel model takes into account 3 flexible modes and is connected to the central body by a revolute joint driven along the x-axis by the SADM. The two solar panels are identical. The joint angular configuration θ is taken into account in the DCM R_{SC/SP_i}. The SADM is the main source of disturbance and is modeled by a local stiffness k_{SP_i}, a viscous friction f_{SP_i} and an internal disturbing torque p^{SP_i}. The overall torque acting on the mechanisms is:

$$u^{SP_i} = k_{SP_i}\delta\theta_i + f_{SP_i}\delta\dot{\theta}_i + p^{SP_i} \tag{5}$$

  where $\delta\theta_i$ and $\delta\dot{\theta}_i$ are obtained integrating the relative acceleration $\delta\ddot{\theta}_i$ of SP_i with respect to S/C. The two coefficients k_{SP_i}, f_{SP_i} are contained in the matrices: $\mathbf{K}_{SP_i} = [f_{SP_i}, k_{SP_i}]$.
- *Antenna (ANT).* The antenna is modeled as a rigid body described by its mass M_{ANT} and its inertia matrix I_{ANT} at the node N_{20} in its local frame aligned with the S/C reference frame. The LOS direction of the antenna therefore coincides with the z-axis of the global reference frame $\mathcal{R}_{S/C}(P_1,\ \mathbf{x},\ \mathbf{y},\ \mathbf{z})$.
- *T-truss structure (T_{str}).* This 36×36 block is the 6 input - 6 output port model described in Section 3.1. The 6 connection points are N_1, N_2, N_3, N_4 (with the parent central body), N_{17} and N_{20} (with the child antenna and PMAs). Since it is composed of 65 flexible beams and since the SDT analytical model of a beam is a 20-th order model, this block is a 1300-th order model.

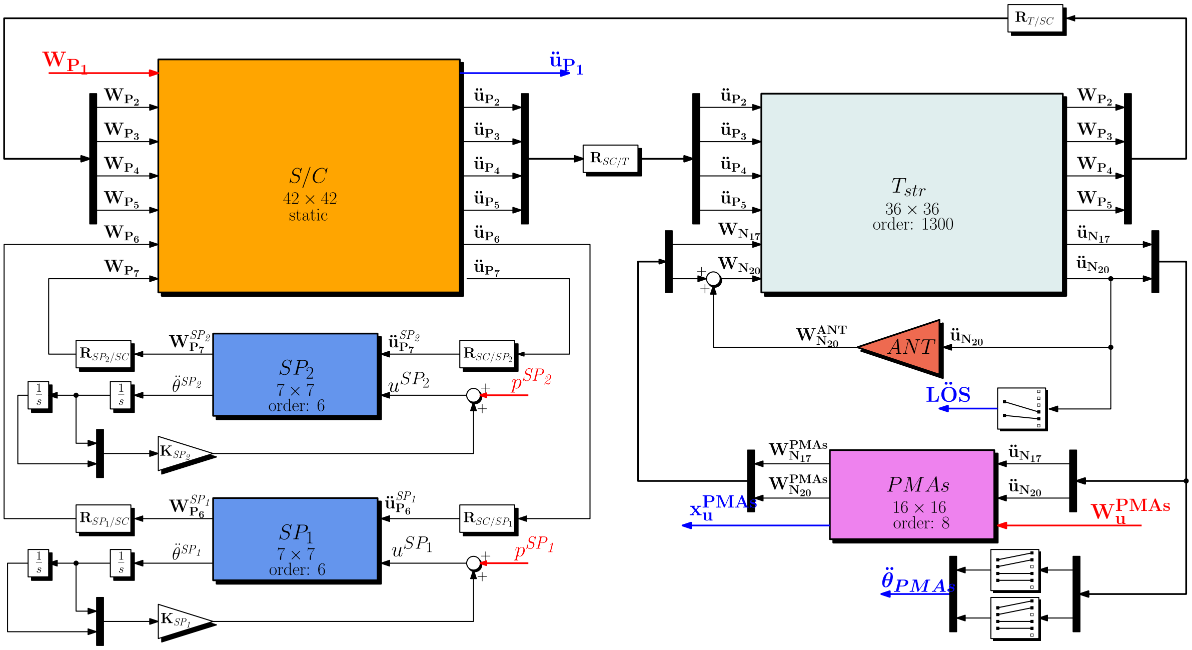

Fig. 11. Open Loop System of the spacecraft in Fig. 8.

- *4 PMAs subsystem* (*PMAs*). This 16×16, 8-th order block embeds the 4 PMAs as described in 3.2. The positioning of these PMAs at node N_{20} and N_{17} has been selected to maximize the control effect over the orientation of the LOS. Thanks to the use of two couples of PMAs acting in the same direction, the control system is able to control the elevation and the azimuth of the LOS and the 2 translations in the plane orthogonal to the LOS.

The data of all spacecraft sub-components can be found in Appendix, Table 6.

The full order model of the whole system is thus a 1324-th order model. Its 20 outputs $\mathbf{y}$, seen in blue in Fig. 11 are:

- **LÖS**: 2×1 vector with LOS elevation and azimuth angular accelerations. This is one of the parameters taken into account in the performance index of the co-design,
- $\mathbf{x_u^{PMAs}}$: 4×1 vector of the linear internal displacements of the 4 PMAs.
- $\mathbf{\ddot{u}_{P_1}}$: 6×1 acceleration dual vector of the center of mass of the central body,
- $\ddot{\theta}_{\boldsymbol{PMA_s}}$: 8×1 vector of the linear and angular accelerations at nodes N_{17} and N_{20} along and around the $\mathbf{x}$ and $\mathbf{y}$ axes.

The 12 inputs $\mathbf{u}$ of the model, highlighted in red in Fig. 11, are:

- p^{SP_1}, p^{SP_2}: the two internal perturbation torques acting at the revolute joints of the each SADM,
- $\mathbf{W_{P_1}}$: 6×1 wrench vector at the center of mass of the spacecraft P_1,
- $\mathbf{W_u^{PMAs}}$: 4×1 vector of linear forces applied to the system at nodes N_{17} and N_{20} by the four PMAs.

One of the main interest of the SDT lies in the possibility of declaring the various mechanical and geometrical parameters as varying parameters or uncertain parameters. Thus, the LPV model directly computed from the block-diagram description is fully compatible with the MATLAB®robust control toolbox to perform robust performance analyzes and robust control designs. That is particularly relevant during preliminary design of Space systems to face fabrication unpredictable inaccuracies and also uncertainties or misknowledges on some sub-systems whose the design is not finalized. It is all the more relevant for preliminary co-design where some of these parameters are tunable parameters. In this case study, two kinds of parameters are considered:

- the **uncertain parameters**: $\boldsymbol{\delta} = [\delta_{M_{SC}},\ \delta_{I_{yy_{SC}}},\ \delta_{\omega_{1_{SP}}},\ \tau]^T$ composed of normalized ($\in [-1,\ 1]$) uncertainties on the mass of the main spacecraft hub M_{SC}, the inertia along the y-axis of the same body $I_{yy_{SC}}$, the first natural frequency of both solar panels $\omega_{1_{SP}}$ and the angular configuration $\theta \in [-\pi,\ \pm\pi]$ of the solar panels parametrized by $\tau = \tan(\theta/4) \in [-1, 1]$ as introduced in [42,43]. The uncertainty values are defined in Appendix, Table 6,
- the **tunable parameter**: $\boldsymbol{\Theta} = h = h_0(1 + 0.95\,\delta_h)$, the side of the T-truss beam section with:

$$h_0 = 2\,cm \quad \delta_h \in [-1,\ 1]\,. \tag{6}$$

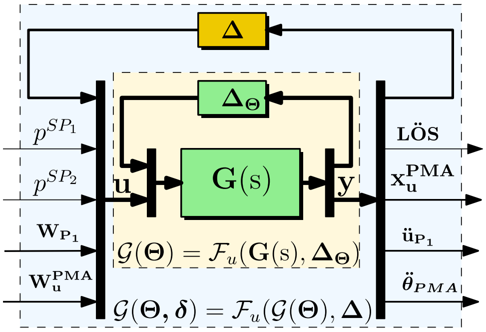

Fig. 12. LFT representation of the LPV full order model $\mathcal{G}(\boldsymbol{\Theta}, \boldsymbol{\delta})$.

Remark. the variation of the beam section side is quite wide. Note that the lower bound (1 mm) is certainly not representative. Constraints on h required for the truss structure (in a stowed configuration) to support launch loads are not considered in this study. The main objective of this paper is to illustrate the interest of the parametric model approach for optimization and co-design purposes.

From the block-diagram model depicted in Fig. 8, the LPV full order model $\mathcal{G}(\boldsymbol{\Theta}, \boldsymbol{\delta})$ is directly computed thanks to the MATLAB®function `ulinearize` and fully characterized by the arguments of the following Linear Fractional Transformation (LFT):

$$\mathcal{G}(\boldsymbol{\Theta}, \boldsymbol{\delta}) = \mathcal{F}_u(\mathcal{G}(\boldsymbol{\Theta}), \boldsymbol{\Delta}) \quad \text{and} \quad \mathcal{G}(\boldsymbol{\Theta}) = \mathcal{F}_u(\mathbf{G}(\mathrm{s}), \boldsymbol{\Delta}_{\boldsymbol{\Theta}}) \tag{7}$$

with $\boldsymbol{\Delta}$ the uncertain parameter block and $\boldsymbol{\Delta}_{\boldsymbol{\Theta}}$ the tunable parameter block defined by:

$$\boldsymbol{\Delta} = \mathrm{diag}\big(\boldsymbol{\Delta}_\tau, \boldsymbol{\Delta}_p\big), \quad \boldsymbol{\Delta}_\tau = \tau\, \mathbf{I_{16}}, \quad \boldsymbol{\Delta}_p = \mathrm{diag}\big(\delta_{M_{SC}}\mathbf{I_3}, \delta_{I_{yy_{SC}}}, \delta_{\omega_{1_{SP}}}\ \mathbf{I_4}\big), \quad \boldsymbol{\Delta}_{\boldsymbol{\Theta}} = \delta_h \mathbf{I_{877}} \tag{8}$$

where $\mathbf{I}_n$ is the identity matrix of size n. This size indicates the number of occurrences of each parameters. Thus the system presents an extremely high number of occurrences for the tunable parameter h, amounting to 877 occurrences.

These upper LFTs $\mathcal{F}_u(.,.)$ can be interpreted by the block-diagram interconnections as depicted in Fig. 12.

3.3.2. System reduction

As mentioned in the previous section, the order of $\mathbf{G}(\mathrm{s})$ is very high (1324). A reduction in the modal state–space representation of $\mathbf{G}(\mathrm{s})$ is thus performed to remove the very slow poles and the high frequency flexible modes based on the following considerations:

- in the modeling of the T-truss structure, the numerous loop closure constraint are solved thanks to the channel inversion operation. Each closed-loop kinematic chain concerns the 6 d.o..fs and leads to 12 poles at 0. But numerical errors during the inversion make that these poles ar not exactly at 0. These very slow poles do not contribute in the input–output transfer of $\mathbf{G}(\mathrm{s})$ and they can be removed by a reduction in the modal realization of $\mathbf{G}(\mathrm{s})$ of all the stable poles with a magnitude lower than 0.01 rad/s. This reduction removes 540 ($= 45 \times 12$ considering the 45 closed-loop kinematic chains inside the T-truss structure) poles. This reduced order model is denoted $\mathbf{G}_{\mathbf{r}_{low}}(\mathrm{s})$,
- very high frequency flexible mode, with a frequency greater than 700 rad/s, are out of the frequency range considered for the active control with the PMAs. They are also reduced in the modal realization of $\mathbf{G}(\mathrm{s})$. This final reduced order model is denoted $\mathbf{G_r}(\mathrm{s})$ and its order is 296.

The goodness of the reduction can be appreciated by comparing the frequency-domain responses of the input–output transfer ($\mathbf{u} \rightarrow \mathbf{y}$) between the full order model $\mathbf{G}(\mathrm{s})$ and the 2 reduced order models $\mathbf{G}_{\mathbf{r}_{low}}(s)$ and $\mathbf{G_r}(\mathrm{s})$, as done in Fig. 13. The magnitude of $\mathbf{G}(\mathrm{s}) - \mathbf{G}_{\mathbf{r}_{low}}(\mathrm{s})$ is totally neglectable, showing the irrelevance of the loop-closure poles, while the magnitude $\mathbf{G}(\mathrm{s}) - \mathbf{G_r}(\mathrm{s})$ shows an acceptable error. The final model $\mathbf{G_r}(s)$ correctly represents the dynamics of the open-loop system in the frequency domain of interest and will be used to perform all further analysis and controller synthesis using the upper linear fractional transformations $\mathcal{G}_r(\boldsymbol{\Theta}) = \mathcal{F}_u(\mathbf{G_r}(\mathrm{s}), \boldsymbol{\Theta})$ for the LPV system and $\mathcal{F}_u(\mathcal{G}_r(\boldsymbol{\Theta}), \boldsymbol{\Delta})$ for the overall uncertain open-loop system.

Nevertheless, the performance robustness analysis proposed in Section 3.7 will consider the model $\mathbf{G}_{\mathbf{r}_{low}}(\mathrm{s})$ with all the flexible modes.

3.4. Closed-loop system

As previously stated, the main objective of this case study is to demonstrate the capability of performing structural and control co-design using parametric models for the flexible appendages, suited for robust analysis. In this context, the reduced open-loop linear model described in the previous section can be augmented with the controllers acting on the system and the pointing performance indexes as shown in Fig. 14.

The closed loop system is composed by two controllers:

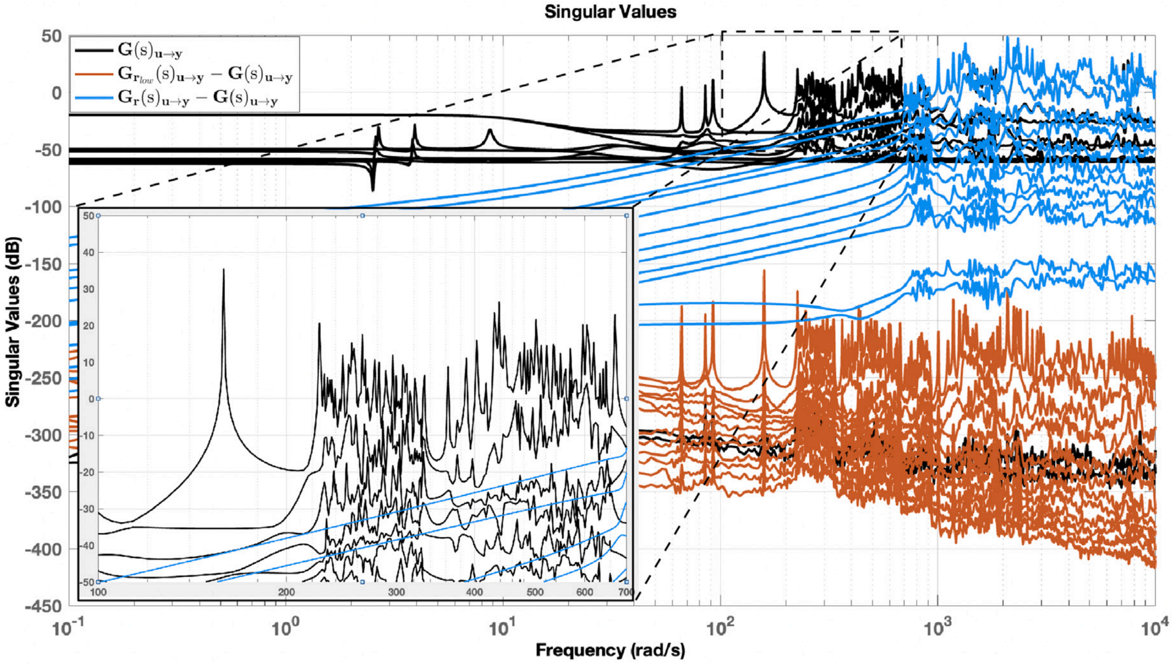

Fig. 13. Comparison on the input–output transfer singular value responses between the full order model $\mathbf{G}_r(s)$, and the reduced order models $\mathbf{G}_{\mathbf{r}_{low}}(s)$, truncated at low frequencies, and $\mathbf{G}_r(s)$, truncated both at low and high frequencies.

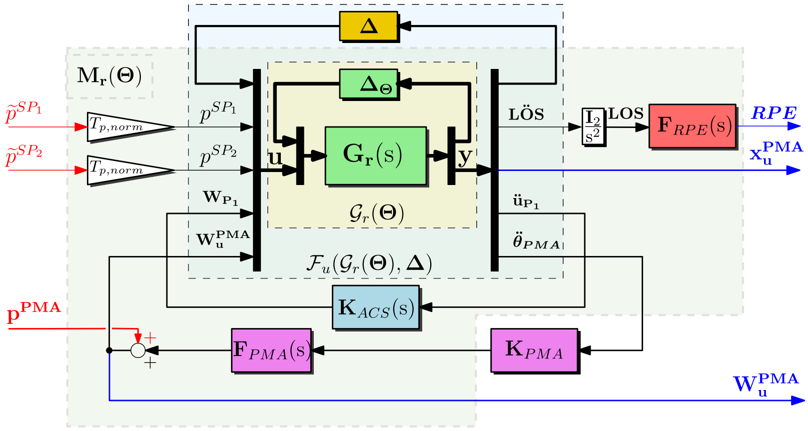

Fig. 14. Closed Loop System for Synthesis.

- *The Attitude Control System ACS*. The ACS implemented for this mission is a basic proportional–derivative (PD) controller aimed at fixing the attitude of the satellite in space.

$$\mathbf{K}_{ACS}(s) = -[\mathbf{0}_{3\times3} \quad \mathbf{I}_3]^T \frac{\mathbf{k}_p + \mathbf{k}_v\, s}{s^2} [\mathbf{0}_{3\times3} \quad \mathbf{I}_3] \tag{9}$$

  $\mathbf{K}_{ACS}(s)$ includes the rigid motion of the whole spacecraft. The decentralized (diagonal) controller gains have been chosen in order to fix the poles of the ACS at a frequency of $\omega_{ACS} = 0.1$ rad/s with a damping of $\xi_{ACS} = 0.7$ assuming the whole spacecraft is rigid:

$$\mathbf{k}_p = \omega^2_{ACS}\mathrm{diag}(\mathbf{J}_{tot}), \qquad \mathbf{k}_v = 2\xi_{ACS}\omega_{ACS}\mathrm{diag}(\mathbf{J}_{tot}) \tag{10}$$

  where $\mathbf{J}_{tot}$ is the total inertia matrix of the satellite computed at point P_1.
- *PMAs Controller*. The controller for the actuator was implemented as by means of the filter $\mathbf{F_{PMAs}}(s)$ and a static gain given by matrix $\mathbf{K_{PMA}}$. $\mathbf{F_{PMAs}}(s)$ is a diagonal 4×4 filter composed of an integrator, required to estimate the velocity from the measured

acceleration, a wash-out filter with a cut-off frequency $\omega_{PMA} = 5\omega_{ACS} = 0.5$ rad/s and a low-pass filter to prevent spillover on neglected flexible modes with a cut-off frequency $\omega_{LP} = 400$ rad/s:

$$\mathbf{F}_{PMA}(\mathrm{s}) = \frac{\mathrm{s}}{\mathrm{s}^2 + 1.4\omega_{PMA}\mathrm{s} + \omega_{PMA}^2} \frac{\omega_{LP}^2}{\mathrm{s}^2 + 1.4\omega_{LP}\mathrm{s} + \omega_{LP}^2}\mathbf{I_4} \,. \tag{11}$$

The fine pointing performance is expressed in form of Relative Performance Error (RPE) as defined in [44]. The RPE index represents the statistics of the instantaneous angular difference between the pointing vector **LOS** and its short-time average in a time interval t_Δ. In the frequency domain this filter corresponds to an high-pass weight [44–46] applied to the system:

$$\mathbf{F}_{RPE}(\mathrm{s}) = \epsilon_{max}^{-1} \frac{t_\Delta \mathrm{s}\,(t_\Delta \mathrm{s} + \sqrt{12})}{(t_\Delta \mathrm{s})^2 + 6(t_\Delta \mathrm{s}) + 12}\mathbf{I_2} \tag{12}$$

where ϵ_{max} is the maximum RPE deviation allowed, which bounds the transfer of the filter. For the present study case the following values were selected: $\epsilon_{max} = 50\,\mu\text{rad}$, $t_\Delta = 3$ ms.

Moreover, the SADM perturbation inputs p^{SP_1} and p^{SP_2} on the system have been normalized by an estimated maximum torque acting on the system, indicated by the upper bound p_{max}: $T_{p,norm} = p_{max} = 0.3820$ Nm. The output $\mathbf{x_u^{PMA}}$ is used to monitor and limit the internal displacements of the 4 PMAs.

Finally the transfer from $\mathbf{p^{PMA}}$ to $\mathbf{W_u^{PMA}}$ is the input sensitivity function of the PMA control loop and can be used to impose stability margins (disc margin).

By assembling all these blocks, the closed-loop LPV system $\mathbf{M_r}(\boldsymbol{\Theta})$ displayed in Fig. 14 is obtained. The uncertainties are added to the model by means of the LFT form $\mathcal{F}_u(\mathbf{M_r}(\boldsymbol{\Theta}), \boldsymbol{\Delta})$. The model can then be augmented with the PMAs controller gains contained in the $\{4 \times 8\}$ scalar matrix $\mathbf{K_{PMA}}$ by means of a lower Linear Fractional Transformation $\mathcal{F}_l\Big(\mathcal{F}_u\big(\mathbf{M_r}(\boldsymbol{\Theta}), \boldsymbol{\Delta}\big), \mathbf{K_{PMA}}\Big)$. The selection of the proper gains to drive the actuation of the PMAs will be the main focus of the structural and control co-design of Section 3.5.

3.5. Robust structure - control co-design

The objective of this study case is to implement a robust co-design of both the T_{str} structure and control laws of the PMAs to maximize pointing performances and minimize the mass $m(\boldsymbol{\Theta})$ of the T-truss structure at the same time. For our study, this means minimizing the reducing the side h of the T-truss beam while constraining the transfer between the normalized SADM perturbation torques $\widetilde{\mathbf{p}} = [\widetilde{p}^{SP_1}, \widetilde{p}^{SP_1}]$ and the normalized RPE index below 1 for any values of the uncertain parameters $\boldsymbol{\delta}$. In addition, two hard constraints are taken into account:

- the internal displacement of each PMA in response to the SDM disturbance torques must be lower that the maximal value $\overline{x}^{\mathbf{PMA}} = 3$ mm,
- the PMA control loop must satisfied stability margins expressed as a disc margin on the input sensitivity function.

Let us consider the LFT closed-loop system $\mathcal{F}_l\Big(\mathcal{F}_u\big(\mathbf{M_r}(\boldsymbol{\Theta}), \boldsymbol{\Delta}\big), \mathbf{K}_{PMA}\Big)$ depicted in Fig. 14, the robust co-design problem reads:

$$\{\widehat{\boldsymbol{\Theta}}, \widehat{\mathbf{K}}_{PMA}\} = \arg \min_{\boldsymbol{\Theta}, \mathbf{K}_{PMA}} m(\boldsymbol{\Theta}) = \arg \min_{h, \mathbf{K}_{PMA}} h \quad \text{such that:} \tag{13}$$

$$\gamma_1 = \max_{\boldsymbol{\Delta}} \left\| \mathcal{F}_l\Big(\mathcal{F}_u\big(\mathbf{M_r}(\boldsymbol{\Theta}), \boldsymbol{\Delta}\big), \mathbf{K}_{PMA}\Big)_{\widetilde{\mathbf{p}} \to \mathbf{RPE}} \right\|_\infty \leq 1 \quad \text{(worst-case pointing performance requirement)} \tag{14}$$

$$\gamma_2 = \max_{\boldsymbol{\Delta}} \left\| \mathcal{F}_l\Big(\mathcal{F}_u\big(\mathbf{M_r}(\boldsymbol{\Theta}), \boldsymbol{\Delta}\big), \mathbf{K}_{PMA}\Big)_{\widetilde{\mathbf{p}} \to \mathbf{x_u^{PMA}}} \right\|_\infty \leq \overline{x}^{\mathbf{PMA}} \quad \text{(worst-case PMA displacement requirement)} \tag{15}$$

$$\gamma_3 = \max_{\boldsymbol{\Delta}} \left\| \mathcal{F}_l\Big(\mathcal{F}_u\big(\mathbf{M_r}(\boldsymbol{\Theta}), \boldsymbol{\Delta}\big), \mathbf{K}_{PMA}\Big)_{\mathbf{p^{PMA}} \to \mathbf{W_u^{PMA}}} \right\|_\infty \leq \gamma_{DM} \quad \text{(worst-case disc margin requirement)} \tag{16}$$

where $\star_{\mathbf{i} \to \mathbf{o}}$ denotes the subsystem from input $\mathbf{i}$ to output $\mathbf{o}$ in the system $\star$.

In the following application $\gamma_{DM} = 1.5$. This value ensures:

- a modulus margin $> 1/\gamma_{DM} = 0.666$,
- a gain margin $> \frac{\gamma_{DM}}{\gamma_{DM} - 1} = 3$ (6 dB),
- a phase margin $> 2 \arcsin \frac{1}{2\gamma_{DM}} = 38.9$ (deg).

The Fig. 15 displays the frequency-domain response relative the pointing performance requirement for the nominal value of the beam side $\boldsymbol{\Theta}_0 = h_0 = 2$ cm without PMA control. One can check that some flexible modes do not meet the constraint.

3.6. Co-design optimization results

The non-smooth robust structured H_∞ problem defined by the performance index (13) and the 3 hard constraints (14), (15) and (16) is solved using MATLAB®'s `systune` routine [35]. In terms of computational efficiency, the optimization takes around 120 min on a standard laptop computer to converge to the solution summarized in Table 4. This yields to a mass reduction of 76% of the T-Truss structure original mass, saving a total of 62.15 kg with respect to the initial design having $m_0 = 81.38$ kg. The impact

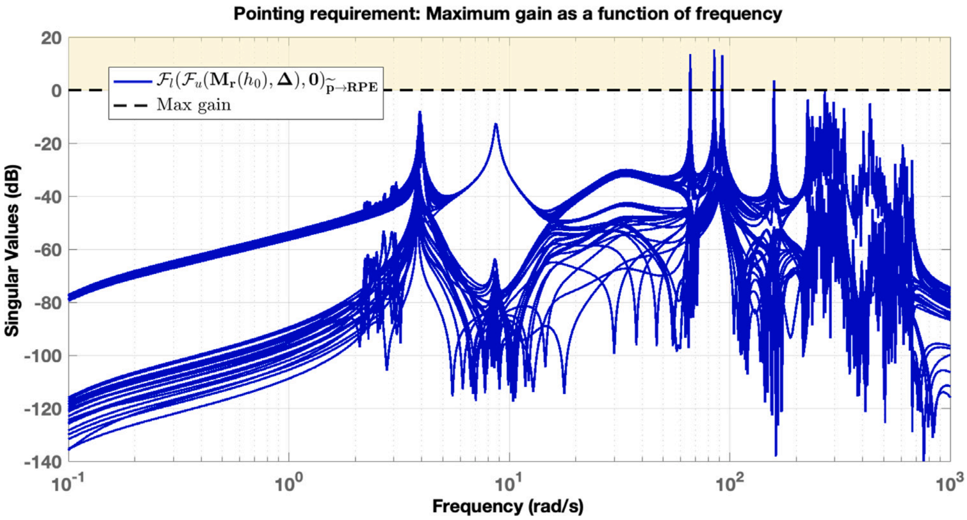

Fig. 15. Frequency-domain illustration of the hard constraint (14) for the nominal side h_0 without PMA control $\mathbf{K}_{PMA} = \mathbf{0}_{4\times 8}$.

Table 4
Co-design results in terms of $\widehat{h}$, structural mass reduction of T_{str} and normalized constraints.

$\widehat{\boldsymbol{\Theta}}$ [cm]	$m(\widehat{\boldsymbol{\Theta}})$ [kg]	m_0 [kg]	$\left(m(\widehat{\boldsymbol{\Theta}}) - m_0\right)/m_0$	γ_1	$\gamma_2/\bar{x}^{\mathbf{PMA}}$	γ_3/γ_{DM}
0.972	19.23	81.38	−76.37%	0.999	0.957	0.999

of the saved T-truss mass/inertia on the whole spacecraft inertia $\mathbf{J}_{tot}$ involved in the tuning of the ACS gains (Eq. (10)) is very small so that the ACS gains do not need to be updated to the new optimal mass/inertia.

The 3 hard constraints are saturated since the weighted γ_i, $i = 1, 2, 3$ values are very close to 1. The frequency domain interpretation of the 3 hard constraints presented in Fig. 16 for several models randomly sampled in the uncertain parametric space highlights the frequencies of interest limiting the performances. The PMA control allows to damp pointing performance critical flexible modes (around 100 rad/s as showcased in Fig. 15 and around 20 rad/s in Fig. 16). thanks to the positivity between the 4 PMAs and the integration of the 4 linear accelerometers but this positivity is limited by the low-pass filter introduced to prevent the spillover on the neglected modes. In addition, this positivity is no more guaranteed regarding the feedback of the 4 angular accelerator (integrated) to the 4 PMAs. That is why the disc margin requirement is very determining for the control design. A more accurate robust performance analysis on the full order model, is presented in the next section.

3.7. Worst-case pointing analysis

Let us consider the closed-loop model described in Section 3.4. Previously, the model $\mathbf{M_r}(\boldsymbol{\Theta})$ displayed in Fig. 14 used for the codesign has been constructed based on the reduced order model $\mathbf{G_r}(s)$. Let us now consider the full order model $\mathbf{M}_{\mathbf{r}low}(\boldsymbol{\Theta})$ obtained just simply changing $\mathbf{G_r}(s)$ by $\mathbf{G}_{\mathbf{r}low}(s)$ in the block diagram interconnection shown in Fig. 14.

In order to fully validate the performance of the optimal solution $\{\widehat{\boldsymbol{\Theta}},\ \widehat{\mathbf{K}}_{PMA}\}$, a worst-case analysis has been implemented on the optimal closed-loop system. The objective is to find the worst-case values of the uncertain parametric vector $\boldsymbol{\delta} = [\delta_{M_{SC}},\ \delta_{I_{yy_{SC}}},\ \delta_{\omega_{1_{SP}}},\ \tau]^T$ for the 3 hard constraints (14), (15) and (16) evaluated on the full-order optimal closed-loop system. The solar panel geometrical configuration parameter $\tau = \tan\theta/4$ is repeated 16 times in the uncertain block $\boldsymbol{\Delta}$ (Eq. (8)) leading to unacceptable computational time using the standard worst-case analysis tools. This problem is circumvented by computing the whole closed-loop model for a given value of τ and by sampling τ on a grid of $N_\tau = 50$ points regularly distributed on $[0,\ 1]$ (or 50 values of θ in $[0,\ 180]°$). This subset has been chosen to account for the symmetric configuration of the model in the $\theta \in [0, 180]°$ and $\theta \in [-180, 0]°$ intervals. By defining $\mathcal{M}(\theta) = \mathcal{F}_u\left(\mathbf{M}_{\mathbf{r}low}(\widehat{\boldsymbol{\Theta}}), \tan(\theta/4)\mathbf{I}_{16}\right)$, the full uncertain closed-loop system associated with the optimal solution reads:

$$\mathcal{M}^{CL}(\theta, \boldsymbol{\Delta}_p) = \mathcal{F}_l\left(\mathcal{F}_u\big(\mathcal{M}(\theta), \boldsymbol{\Delta}_p\big), \widehat{\mathbf{K}}_{PMA}\right) \tag{17}$$

where all the remaining uncertainties on M_{SC}, $I_{yy_{SC}}$ and $\omega_{1_{SP}}$ are contained in the matrix $\boldsymbol{\Delta}_p$.

The objective is thus to solve the 3 μ-analysis problems:

$$\mu_1(\theta) = \max_{\boldsymbol{\Delta}_p} \left\| \mathcal{M}^{CL}(\theta, \boldsymbol{\Delta}_p)_{\widetilde{\mathbf{p}}\to\mathbf{RPE}} \right\|_\infty, \tag{18}$$

$$\mu_2(\theta) = \max_{\boldsymbol{\Delta}_p} \left\| \frac{1}{\overline{x}^{\mathbf{PMA}}} \mathcal{M}^{CL}(\theta, \boldsymbol{\Delta}_p)_{\widetilde{\mathbf{p}}\to\mathbf{x_u^{PMA}}} \right\|_\infty, \tag{19}$$

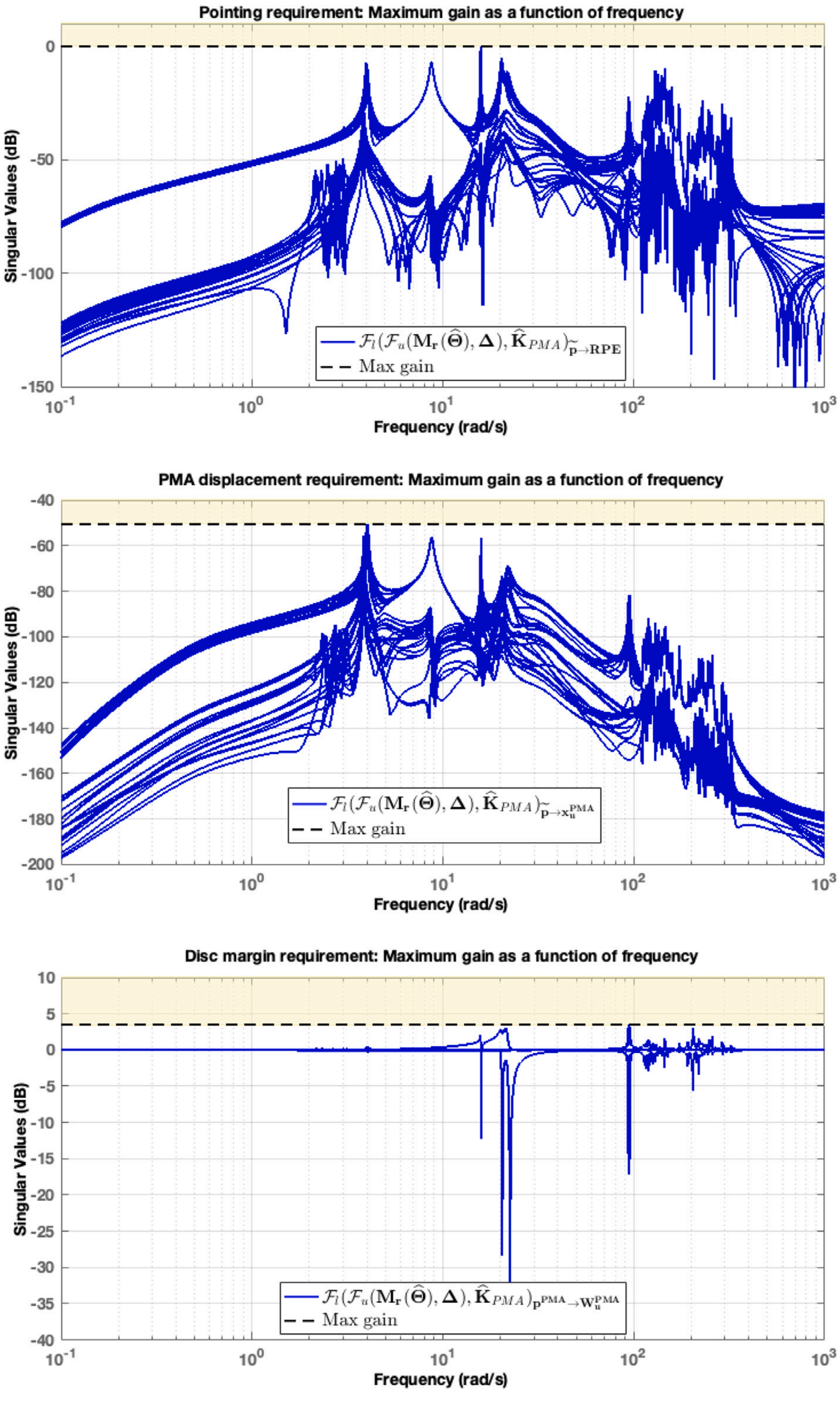

Fig. 16. Frequency-domain illustrations of the hard constraints (14), (15) and (16) for the optimal side $\widehat{\boldsymbol{\Theta}}_0$ and the optimal PMA control $\widehat{\mathbf{K}}_{PMA}$.

Table 5
Worst-case analysis results for the three transfers of interest (θ_{WC} is the worst-case solar panel geometrical configuration).

i	$\max_\theta \overline{\mu}_i(\theta)$	$\theta_{WC} = \arg\max_\theta \overline{\mu}_i(\theta)$ [deg]	$\underline{\mu}_i(\theta_{WC})$	Critical freq. [rad/s]	Worst-case M_{SC} [kg]	Worst-case $I_{yy_{SC}}$ [kg m^2]	Worst-case $\omega_{1_{SP}}$ [rad/s]
1	0.9767	94.5	0.9754	20.4	945	871	2.854
2	0.974563	42.5	0.97234	3.99	720	1100	2.254
3	1.0471	0	1.0469	473.	800	990	2.472

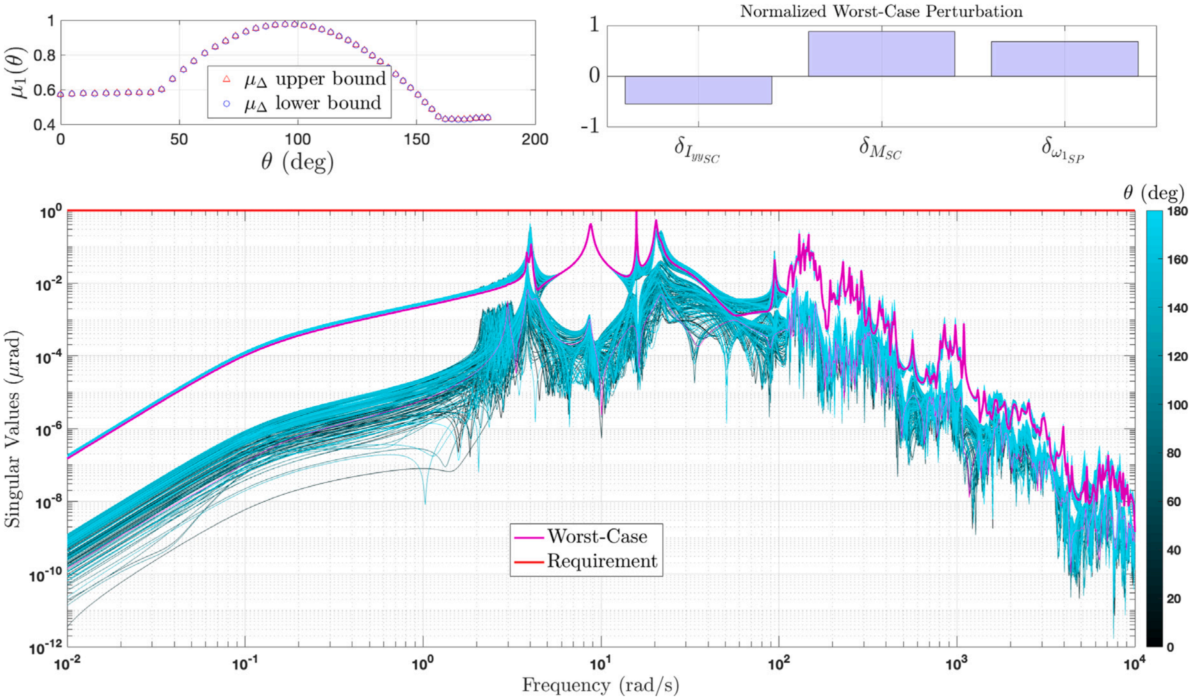

Fig. 17. Worst-case analysis for the pointing performance transfer $\mathcal{M}^{CL}(\theta, \boldsymbol{\Delta}_p)_{\tilde{\mathbf{p}}\to\mathbf{RPE}}$ as a function of θ. On the top part of the figure, the μ-bounds are displayed together with the worst-case parameter combinations. Down below, the singular values of the transfer and its worst-case are showcased.

$$\mu_3(\theta) = \max_{\boldsymbol{\Delta}_p} \left\| \frac{1}{\gamma_{DM}} \mathcal{M}^{CL}(\theta, \boldsymbol{\Delta}_p)_{\tilde{\mathbf{p}}\to\mathbf{W}_\mathbf{u}^{\mathbf{PMA}}} \right\|_\infty . \tag{20}$$

For the $i = 1, 2, 3$ and for the N_τ values of τ (or θ), these μ-analysis problems $\mu_i(\theta)$ are solved by means of the `wcgain` routine in MATLAB®'s *Robust Control Toolbox* [30]. This function provides an upper bound $\overline{\mu}_i(\theta)$ and a lower bound $\underline{\mu}_i(\theta)$ of $\mu_i(\theta)$. The worst-case parametric configuration is associated to this lower bound. The function also returns the critical frequency where the worst gain occurs. The worst-case performances and the associated worst-case parametric combinations are summarized in Table 5. One can check that the gaps between the upper bounds and the lower bounds are very small for the 3 transfers of interest showing that the worst-case performance is accurately evaluated. The hard constraints for the pointing performance ($i = 1$) and the PMAs displacements ($i = 2$) are thus validated on the full order model. The hard constraint on the disc margin ($i = 3$) is slightly above 1 but can be considered as satisfying.

In Fig. 17 a complete representation on the worst-case analysis results is presented for the main transfer of interest, i.e. the pointing performance ($\mu_1(\theta)$), in terms of its μ-bounds as a function of θ, the frequency-domain response and the worst case parameter combination. It can be seen that the μ analysis identified the two bounds close to each other and always with a value below the unity, successfully validating the robustness of the design. Moreover, it can be remarked that the bounds show a visible trend, which justifies the choice of a relative low number of N_τ for this analysis. Furthermore, the study of the singular value responses reveals that the worst-case frequency response of the system remains always below requirement.

4. Conclusions

This paper aimed at introducing new analytical tools to model large complex truss structures for space applications in the TITOP/NINOP framework with the specific objective of developing models for structure/control co-design and robust analysis and control. A series of 2D mechanisms block has been introduced to build a unitary 3D cubic element which serves as a building block for truss structures in a sub-structuring approach. The analysis displayed the potentialities of the approach, as large structures

Table 6
Spacecraft mechanical characteristics.

	Parameter	Description	Value & Uncertainty
Spacecraft S/C	P_1	Spacecraft C.o.G.	[0, 0, 0] m
	M_{SC}	Mass	800 kg ± 20%
	$\begin{bmatrix} I_{xx_{SC}} & I_{xy_{SC}} & I_{xz_{SC}} \\ & I_{yy_{SC}} & I_{yz_{SC}} \\ & & I_{zz_{SC}} \end{bmatrix}$	Inertia in $\mathcal{R}_{SC}$ frame	$\begin{bmatrix} 1000 & 0 & 0 \\ & 1000 \pm 20\% & 0 \\ & & 200 \end{bmatrix} \mathrm{kg\,m^2}$
Solar Panels SP	$\mathbf{r}_{OG}^{SP}$	Solar panel C.o.G. in $\mathcal{R}_{SP}$	$[0; -2; 0.03]$ m
	M_{SP_1}	Mass	80 kg
	$\begin{bmatrix} I_{xx_{SP}} & I_{xy_{SP}} & I_{xz_{SP}} \\ & I_{yy_{SP}} & I_{yz_{SP}} \\ & & I_{zz_{SP}} \end{bmatrix}$	Inertia in $\mathcal{R}_{SP}$	$\begin{bmatrix} 80 & 0 & -0.1 \\ & 20 & 22 \\ & & 100 \end{bmatrix}$ kg m^2
	$[\omega_{1_{SP}}, \omega_{2_{SP}}, \omega_{3_{SP}}]$	Flexible modes' frequencies	[2.51 ± 20%, 3.77, 9.42] rad/s
	$[\xi_{1_{SP}}, \xi_{2_{SP}}, \xi_{3_{SP}}]$	Flexible modes' damping	0.003
	$\mathbf{L}_{SP}$	Modal participation factors	$\begin{bmatrix} -0.002 & -1.5 & -5 & 14 & 0.02 & -0.01 \\ 5 & 1 & -0.1 & 0 & 2 & 15 \\ 0.3 & 0.002 & 0.03 & -0.02 & 3.2 & -0.2 \end{bmatrix}$
HPP Antenna ANT	M_{ANT}	Mass	20 kg
	$\begin{bmatrix} I_{xx_{ANT}} & I_{xy_{ANT}} & I_{xz_{ANT}} \\ & I_{yy_{ANT}} & I_{yz_{ANT}} \\ & & I_{zz_{ANT}} \end{bmatrix}$	Inertia in $\mathcal{R}_{ANT}$	$\begin{bmatrix} 1.32 & 0 & 0 \\ & 1.32 & 0 \\ & & 2.5 \end{bmatrix} \mathrm{kg\,m^2}$
PMAs	M^B	Casing mass	0.5 kg
	$\begin{bmatrix} I_{xx_B} & I_{xy_B} & I_{xz_B} \\ & I_{yy_B} & I_{yz_B} \\ & & I_{zz_B} \end{bmatrix}$	Casing Inertia in the PMA frame at G	$\begin{bmatrix} 5e-3 & 0 & 0 \\ & 5e-3 & 0 \\ & & 1.6e-4 \end{bmatrix}$ kg m^2
	$\mathbf{r}_{0G}^{PMA}$	PMA C.o.G. in $\mathcal{R}_B$	$[0; 0.05; 0]$ m
	$\mathbf{r}_{0P}^{PMA}$	PMA connection point in $\mathcal{R}_B$	$[0; 0; 0]$ m
	$\mathbf{v}$	Spring–damper direction in $\mathcal{R}_B$	$[0; 1; 0]$ m
	m_p	Proof mass	0.1 kg
	k_p	Spring stiffness	10 N/m
	d_p	Damper	1.4 Ns/m

composed by a high number of beam elements can be easily assembled by using blocks of decreasing complexity. In addition, a full validation campaign by comparison with Nastran validated the representativeness of these models.

A case study was then introduced to represent the strengths of the TITOP/NINOP approach in performing robust structure/control co-design in presence of parametric uncertainties. A complex 3D truss structure was built using the previously introduced cube elements and attached to a spacecraft to act as support for an high precision antenna. The objective of the co-design was to reduce the structural mass of the system while satisfying a fine pointing requirement. This study case highlighted the potential of these analytical blocks in performing complex multi disciplinary optimization problems. The direct co-design using structured H_∞ control synthesis allowed for computational cost reduction and brought to a mass saving of almost 76% of the original structural mass, while coping with stringent pointing performances and a large set of uncertainties in the mechanical design parameters. The main conclusion of this work is that it is possible to develop knowledge-based models for complex truss structures with an analytical dependence on the sizing, variable or uncertain parameters. These models can be directly used for robust design, robustness analysis or parametric optimization, thus simplifying model uncertainty quantification and model reduction in the overall control/structure integrated design process.

Declaration of competing interest

The authors declare that they have no known competing financial interests or personal relationships that could have appeared to influence the work reported in this paper.

Appendix

See Tables 6 and 7.

Table 7
Definition of connection points for the spacecraft sub-systems in the spacecraft reference frame $\mathcal{R}_{SC}(P_1,\ x,\ y,\ z)$.

Description	Point	Coordinates	Unit	Description	Point	Coordinates	Unit
T_{str} connection to S/C at Node 1	P_2	[−0.5, −0.5, 1]	m	T_{str} connection to S/C at Node 4	P_5	[−0.5, 0.5, 1]	m
T_{str} connection to S/C at Node 2	P_3	[0.5, −0.5, 1]	m	Solar Panel 1 SP_1 connection to S/C	P_6	[1, 0, 0]	m
T_{str} connection to S/C at Node 3	P_4	[0.5, 0.5, 1]	m	Solar Panel 2 SP_2 connection to S/C	P_7	[−1, 0, 0]	m

References

[1] C. Dennehy, O.S. Alvarez-Salazar, Spacecraft Micro-Vibration: A Survey of Problems, Experiences, Potential Solutions, and Some Lessons Learned, Tech. Rep. NASA/TM-2018-220075, NASA, 2018.

[2] V. Preda, J. Cieslak, D. Henry, S. Bennani, A. Falcoz, Robust microvibration mitigation and pointing performance analysis for high stability spacecraft, Internat. J. Robust Nonlinear Control 28 (18) (2018) 5688–5716, http://dx.doi.org/10.1002/rnc.4338.

[3] F. Sanfedino, V. Preda, V. Pommier-Budinger, D. Alazard, F. Boquet, S. Bennani, Robust active mirror control based on hybrid sensing for spacecraft line-of-sight stabilization, IEEE Trans. Control Syst. Technol. 29 (1) (2021) 220–235, http://dx.doi.org/10.1109/TCST.2020.2970658.

[4] F. Sanfedino, D. Alazard, V. Preda, D. Oddenino, Integrated modeling of microvibrations induced by Solar Array Drive Mechanism for worst-case end-to-end analysis and robust disturbance estimation, Mech. Syst. Signal Process. 163 (2022) 108168, http://dx.doi.org/10.1016/j.ymssp.2021.108168.

[5] R.J. Theodore, A. Ghosal, Comparison of the assumed modes and finite element models for flexible multilink manipulators, Int. J. Robot. Res. 14 (2) (1995) 91–111, http://dx.doi.org/10.1177/027836499501400201.

[6] H. Holzer, Analysis of Torsional Vibration, Springer, Berlin, 1921.

[7] N. Myklestad, New method of calculating natural modes of coupled bending-torsion vibration of beams, Trans. ASME 67 (1) (1945) 61–67, http://dx.doi.org/10.2514/8.11116.

[8] T. Tan, A. Yousuff, L. Bahar, M. Konstantinidis, A modified finite element-transfer matrix for control design of space structures, Comput. Struct. 36 (1) (1990) 47–55, http://dx.doi.org/10.1016/0045-7949(90)90173-Y.

[9] X. Rui, J. Zhang, Q. Zhou, Automatic deduction theorem of overall transfer equation of multibody system, Adv. Mech. Eng. 6 (2014) 378047, http://dx.doi.org/10.1155/2014/378047.

[10] W.C. Hurty, Dynamic analysis of structural systems using component modes, AIAA J. 3 (4) (1965) 678–685, http://dx.doi.org/10.2514/3.2947.

[11] R.H. MacNeal, A hybrid method of component mode synthesis, Comput. Struct. 1 (4) (1971) 581–601, http://dx.doi.org/10.1016/0045-7949(71)90031-9.

[12] R.M. Hintz, Analytical methods in component modal synthesis, AIAA J. 13 (8) (1975) 1007–1016, http://dx.doi.org/10.2514/3.60498.

[13] K. Holm-Jørgensen, S.R. Nielsen, A component mode synthesis algorithm for multibody dynamics of wind turbines, J. Sound Vib. 326 (3–5) (2009) 753–767, http://dx.doi.org/10.1016/j.jsv.2009.05.007.

[14] D.-M. Tran, Reduced models of multi-stage cyclic structures using cyclic symmetry reduction and component mode synthesis, J. Sound Vib. 333 (21) (2014) 5443–5463, http://dx.doi.org/10.1016/j.jsv.2014.06.004.

[15] J.-x. Yu, Y. Xia, W. Lin, X.-q. Zhou, Element-by-element model updating of large-scale structures based on component mode synthesis method, J. Sound Vib. 362 (2016) 72–84, http://dx.doi.org/10.1016/j.jsv.2015.10.019.

[16] A. Girard, N. Roy, Structural Dynamics in Industry, Wiley, 2008.

[17] M. Pascal, Dynamics analysis of a system of hinge-connected flexible bodies, Celestial Mech. 41 (1) (1987) 253–274, http://dx.doi.org/10.1007/BF01238763.

[18] C. Cumer, D. Alazard, A. Grynagier, C. Pittet-Mechin, Codesign mechanics/attitude control for a simplified AOCS preliminary synthesis, in: 9th International ESA Conference on Guidance, Navigation & Control Systems (GNC 2014), 2014.

[19] N. Guy, D. Alazard, C. Cumer, C. Charbonnel, Dynamic modeling and analysis of spacecraft with variable tilt of flexible appendages, J. Dyn. Syst. Meas. Control 136 (2) (2014) 021020, http://dx.doi.org/10.1115/1.4025998.

[20] K.H. Tantawi, D. Alazard, C. Cumer, Linear dynamic modeling of spacecraft with various flexible appendages, IFAC Proc. Vol. 41 (2) (2008) 11148–11153, http://dx.doi.org/10.3182/20080706-5-KR-1001.01889.

[21] D. Alazard, J.A. Perez, C. Cumer, T. Loquen, Two-input two-output port model for mechanical systems, in: AIAA Guidance, Navigation, and Control Conference, p. 1778, http://dx.doi.org/10.2514/6.2015-1778.

[22] H. Murali, C. Toglia, F. Ankersen, L. Massotti, Mechanical-Attitude Controller Co-design of Large Flexible Space Structures, 2015, http://dx.doi.org/10.1007/978-3-319-17518-8_38.

[23] J.A. Perez, D. Alazard, T. Loquen, C. Cumer, C. Pittet, Linear dynamic modeling of spacecraft with open-chain assembly of flexible bodies for ACS/structure co-design, in: Advances in Aerospace Guidance, Navigation and Control, Springer, 2015, pp. 639–658, http://dx.doi.org/10.1007/978-3-319-17518-8_37.

[24] J.A. Perez, C. Pittet, D. Alazard, T. Loquen, C. Cumer, A flexible appendage model for use in integrated control/structure spacecraft design, IFAC-PapersOnLine 48 (9) (2015) 275–280, http://dx.doi.org/10.1016/j.ifacol.2015.08.096.

[25] J. Chebbi, V. Dubanchet, J.A. Perez Gonzalez, Linear dynamics of flexible multibody systems: A system-based approach, Multibody Syst. Dyn. 41 (1) (2016) 75–100, http://dx.doi.org/10.1007/s11044-016-9559-y.

[26] F. Sanfedino, D. Alazard, V. Pommier-Budinger, A. Falcoz, F. Boquet, Finite element based N-port model for preliminary design of multibody systems, J. Sound Vib. 415 (2018) 128–146, http://dx.doi.org/10.1016/j.jsv.2017.11.021.

[27] D. Alazard, F. Sanfedino, Satellite dynamics toolbox for preliminary design phase, in: 43rd Annual AAS Guidance and Control Conference, vol. 30, 2020, pp. 1461–1472.

[28] D. Alazard, F. Sanfedino, Satellite Dynamics Toolbox library SDTlib - User's Guide, 2021, URL https://personnel.isae-supaero.fr/daniel-alazard/matlab-packages/satellite-dynamics-toolbox.html?lang=fr.

[29] P.G. Maghami, K.B. Lim, Synthesis and control of flexible systems with component-level uncertainties, J. Dyn. Syst. Meas. Control 131 (5) (2009) 051005, http://dx.doi.org/10.1115/1.3155010, arXiv:https://asmedigitalcollection.asme.org/dynamicsystems/article-pdf/131/5/051005/5659161/051005_1.pdf.

[30] G. Balas, R. Chiang, A. Packard, M. Safonov, Robust Control Toolbox user's guide, The Math Works, Inc., 2007.

[31] P. Maghami, S. Gupta, K. Elliot, S. Joshi, Integrated controls-structures design methodology: Redesign of an evolutionary test structure, J. Guid. Control Dyn. 19 (2000) http://dx.doi.org/10.2514/3.21621.

[32] L.A. Schmit, Structural design by systematic synthesis, in: In Proceedings of the Second National Conference on Electronic Computation, ASCE, 1960.

[33] R.T. Haftka, Automated Procedure for Design of Wing Structures to Satisfy Strength and Flutter Requirements, NASA Langley Research Center TN-D-7264, Hampton, VA, 1973.

[34] A. Falcoz, M. Watt, M. Yu, A. Kron, P.P. Menon, D. Bates, F. Ankersen, L. Massotti, Integrated control and structure design framework for spacecraft applied to biomass satellite, IFAC Proc. Vol. 46 (19) (2013) 13–18, http://dx.doi.org/10.3182/20130902-5-DE-2040.00051.

[35] P. Gahinet, P. Apkarian, Structured H_∞ synthesis in MATLAB, IFAC Proc. Vol. 44 (1) (2011) 1435–1440, http://dx.doi.org/10.3182/20110828-6-IT-1002.00708.

[36] D. Alazard, T. Loquen, H. De Plinval, C. Cumer, Avionics/control co-design for large flexible space structures, in: AIAA Guidance, Navigation, and Control (GNC) Conference, 2013, p. 4638, http://dx.doi.org/10.2514/6.2013-4638.

[37] Y. Denieul, J. Bordeneuve-Guibé, D. Alazard, C. Toussaint, G. Taquin, Multicontrol surface optimization for blended wing?body under handling quality constraints, J. Aircr. (2018) 1–14, http://dx.doi.org/10.2514/1.C034268, https://arc.aiaa.org/doi/10.2514/1.C034268.

[38] G.J. Balas, Robust Control of Flexible Structures: Theory and Experiments (Ph.D. thesis), California Institute of TechnologyT, 1990, URL https://resolver.caltech.edu/CaltechETD:etd-10252002-160528.

[39] M. Campbell, E. Crawley, Uncertainty modeling for structural control analysis and synthesis, 1996, http://dx.doi.org/10.2514/6.1996-1486.

[40] K.B. Lim, Structured Uncertainty Bound Determination From Data for Control and Performance Validation, Tech. Rep. NASA/TM-2003-212441, National Aeronautics and Space Administration, Langley Research Center - Hampton, Virginia 23681-2199, 2003.

[41] F. Bourgault, Model Uncertainty and Performance Analysis for Precision Controlled Space Structures (Master's thesis), Massachusetts Institute of Technology, 2000.

[42] N. Guy, D. Alazard, C. Cumer, C. Charbonnel, Dynamic modeling and analysis of spacecraft with variable tilt of flexible appendages, J. Dyn. Syst. Meas. Control 136 (2) (2014) http://dx.doi.org/10.1115/1.4025998.

[43] V. Dubanchet, Modeling and Control of a Flexible Space Robot to Capture a Tumbling Debris (Ph.D. thesis), Ecole Polytechnique, Montreal (Canada), 2016.

[44] T. Ott, A. Benoit, P. Van den Braembussche, W. Fichter, ESA pointing error engineering handbook, in: 8th International ESA Conference on Guidance, Navigation & Control Systems, 2011, p. 17.

[45] M. Pittelkau, Pointing error definitions, metrics, and algorithms, in: Proceedings of the AAS/AIAA Astrodynamics Specialist Conference, American Astronautical Society, 2003, pp. 901–920.

[46] T. Ott, W. Fichter, S. Bennani, S. Winkler, Precision pointing H_∞ control design for absolute, window-, and stability-time errors, CEAS Space J. 4 (1) (2013) 13–30, http://dx.doi.org/10.1007/s12567-012-0028-z.